I&EC research
Industrial & Engineering Chemistry Research

Article

pubs.acs.org/IECR

Modeling the Effects of Concentration of Solid Nanoparticles in Liquid Feedstock Injection on High-Velocity Suspension Flame Spray Process

Mahrukh Mahrukh,[†,‡] Arvind Kumar,[§] Sai Gu,[*,∥] Spyros Kamnis,[#] and Ebrahim Gozali[⊥]

[†]School of Energy, Environment & Agrifood, Cranfield University, Cranfield, Bedfordshire, MK43 0AL, U.K.

[‡]Department of Mechanical Engineering, NED University of Engineering & Technology, University Road, 75270 Karachi, Pakistan

[§]Department of Mechanical Engineering, Indian Institute of Technology, Kanpur 208016, India

[∥]Department of Chemical and Process Engineering, Faculty of Engineering and Physical Sciences, University of Surrey, Guildford, GU2 7XH, U.K.

[⊥]School of Engineering Sciences, University of Liverpool, Liverpool L69 3BX, U.K.

[#]Monitor Coatings Limited, 2 Elm Road, North Shields, Tyne & Wear, NE29 8SE, U.K.

ABSTRACT: This paper presents the effects of the concentration of solid nanoparticles in the liquid feedstock injection on the high-velocity suspension flame spray (HVSFS) process. Four different concentrations of solid nanoparticles in suspension droplets with various droplet diameters are used to study gas dynamics, vaporization rate, and secondary breakup. Two types of injections, viz. surface and group, are used. The group-type injection increases the efficiency of droplet disintegration and the evaporation process and reduces the gas cooling. The initiation of the fragmentation process is difficult for small droplets carrying a high concentration of nanoparticles. Also, smaller droplets undergo rapid vaporization, leaving clogs of nanoparticles in the middle of the barrel. For larger droplets, severe fragmentation occurs inside the combustion chamber. For a higher concentration of nanoparticles, droplets exit the gun without complete evaporation. The results suggest that, in coating applications involving a higher concentration of nanoparticles, smaller droplet sizes are preferred.

1. INTRODUCTION

The technology of the high-velocity suspension flame spray (HVSFS) process is an upgraded version of the conventional high-velocity oxygen fuel (HVOF) thermal spraying process.[1] HVOF uses metallic powder particles for the spraying process, and with modifications in the spraying system, it can serve for ceramic particles.[2] One of the modifications in the HVOF process is to use liquid feedstock (suspension) instead of dry powders, to inject suspended nanoparticles. A suspension is a mixture of solid nanoparticles suspended in a liquid medium consisting, for instance, of water, ethanol, or isopropanol.[3,4] This dispersion mechanism in a liquid carrier provides adequate flowability to nanoparticles, which cannot be handled by conventional gas carrier based feeding systems.[4] Liquid feedstock spraying, in general, could offer unique opportunities for designing and fabricating complex material architectures with controlled and hierarchical microstructures.[4−6] The suspension spraying works well for several applications including thermal barrier coatings, tribofunctional and wear-resistant coatings, biofunctional coatings, fuel cell development, and coatings for catalytically active surfaces.[7−10] Recent examples include the fabrication of thermoelectric modules and solar cells made from thermally sprayed silicon wafers.[11] Further, liquid feedstock spraying could lead to advancements in the spraying industry to spray nanoparticles to obtain a dense and thick coating with excellent bond strength.[4,10,12−14]

In the HVSFS process, premixed fuel and oxygen are injected in the combustion chamber (CC) through inlet holes (or injection ports). The hot gas accelerates through the nozzle and passes through the convergent−divergent (C−D) section. The coating material in suspension form, consisting of fine particles (nanometric, or a few micrometers in size) dispersed in an organic solvent, is injected into the main gas flow. This suspension of micrometer-sized droplets then travels in the high-temperature flow region inside the torch. During the traveling path these liquid droplets break up due to large relative velocity between gas and liquid phases and, subsequently, evaporate and combust along their trajectory.[15−18] The remaining solid part of the spray or fine agglomerates of nanoparticles are accelerated and deposited on a substrate.

In studies reported in ref 19, the HVSFS process based on nanosize powder suspension resulted in very small and well-flattened lamellae (thickness range 100 nm to 1 μm). The coating exhibited low porosity as compared to air plasma spraying (APS) and HVOF coating and showed higher protectiveness. The sliding wear resistance of HVSFS coatings is much greater than that of conventionally sprayed coatings.[19] It is due to small lamellae and smaller interlamellar crystal size that allows microscale plastic deformability, thus forming much more stable and protective tribofilms than conventional coatings.[19] In another study, the effects of varied injection

Received: October 25, 2015
Revised: January 15, 2016
Accepted: February 3, 2016
Published: February 3, 2016

DOI: 10.1021/acs.iecr.5b03956
Ind. Eng. Chem. Res. 2016, 55, 2556−2573

parameters on the final coatings are analyzed by using different injection systems.[1] The injection nozzle was replaced, and two different suspension feeder systems were used: (i) mechanical pumping of the suspension using a piston pump (type I) and (ii) suspension transport through a pressure vessel that is operated with compressed nitrogen gas (type II). Varied nozzle diameters of 1.2 (standard nozzle), 0.7, 0.5, and 0.4 mm (inserts) were designed to examine the influence of the nozzle diameter on the spraying process. It was evaluated that a type II feeder with a smaller nozzle injection diameter improves the heating/melting of zirconia particles, as it delivers low flow rates with the improved shape of the suspension spray jet.[1]

The HVSFS spray technology is the most convenient way of using nanoparticles for thermal spraying. The injection mechanism used for liquid feedstock is different from the conventional powder spraying setup.[1] Furthermore, it includes multiple stages of droplet disintegration, liquid vaporization, and heat transfer between nanoparticles and the surrounding hot gas.[18] Therefore, understanding the liquid feedstock behavior in such a complex system becomes crucial for its further development. Researchers are attempting to analyze the above-mentioned complex phenomena to suggest the link between them.[1,4,10,12,15,18,20−22] Modeling and numerical methods are employed to understand the flow physics related to a suspension mixture containing nanoparticles of various concentrations.[15,16]

Numerical analysis of the HVSFS process is not well documented in the literature. The modeling of an HVOF system is presented by Dongmo et al.[17] in which they discuss the effects of process parameters, such as gas flow rates, stoichiometric oxy/fuel ratio, and nozzle design, on in-flight properties of particles. Dongmo et al.[15] also modeled the HVOF and HVSFS thermal spraying phenomena. They analyzed combustion and gas dynamics in an industrial TopGun-G torch (GTV, Düsseldorf, Germany), by using three-dimensional computational fluid dynamics (CFD) modeling. They found that liquid feedstock injection is capable of processing submicrometer and nanosize particles for achieving highly dense coatings having fine structures with superior mechanical and physical properties. They concluded that the modification in the torch's CC (by giving it a conical shape) increases the process efficiency, and helps to avoid nanoparticle contact with the CC walls.

Moreover, Dongmo et al.[16] discussed the HVSFS process in which both liquid ethanol droplets (300 μm) and solid titania particles (0.5−50 μm) are injected from the gun inlet as separate discrete phases. It is revealed that, due to the difference in the thermophysical properties of solid nanoparticles and ethanol droplets, they move with different velocities inside the thermal spray torch. This study ignored the effect of nanoparticle loading on properties of pure ethanol, its evaporation process, and the consequent effects on combustion gas dynamics. The evaporation of ethanol droplets shows significant cooling of the combustion gases at a 0° angle of injection. Injection at an angle of 30° improves the rate of evaporation for ethanol droplets inside the CC, and the cooling is reduced. The disadvantages of angular injection highlighted in this study are the impingement of droplets and particles on the CC walls; thereby they may deposit on the torch internal walls and damage them.

The HVSFS process is modeled by Gozali et al.[5,6] to understand the strategies of optimizing the recent technology. They highlighted that using water, ethanol, and their mixture as a solvent for liquid feedstock tends to cool the HVOF flame and thereby decrease its temperature and heating value. Moreover, the axial injection of the liquid feedstock into the CC can give better results when compared to injecting particles in the barrel or at the exit of the torch. In a recent work[23] the injection of liquid feedstock carrying multicomponent droplets of ethanol and water inside the HVSFS process is modeled. Varied compositions of ethanol and water mixture in the liquid feedstock suspension are studied to see the effects on the temperature and on the velocity of the hot gas. This study showed that organic solvents experience rapid evaporation during the HVSFS process while the aqueous solution and its mixtures undergo a lower rate of evaporation. In a recent work Gozali et al.[24] studied the effect of solid nanoparticle concentrations on the liquid droplet breakup and evaporation processes. They concluded that the rates of evaporation for homogeneous and nonhomogeneous feedstock droplets are quite different in the HVOF torch.

In the HVSFS process, the thermophysical properties of the suspension, such as density, viscosity, specific heat, thermal conductivity, and surface tension, are altered with varying nanoparticle concentration.[24−29] As a result, assigning pure solvent properties or averaging solid and liquid properties for a suspension may produce significant errors in numerical simulations. For example, the location of evaporation of the homogeneous solvent (ethanol) might be different from that of the nonhomogeneous suspension (ethanol-carrying nanoparticles). It will, in turn, influence the characteristics of the liquid droplets in the HVSFS field that governs the coating quality. In numerical simulations, the nanoparticles are typically prescribed as new Lagrangian entities.[15,16,30] Hence, in-flight liquid droplets' current position, velocity, and temperature values are assigned to the newly released (or agglomerated) solid particles as initial conditions after complete evaporation of liquid droplets.[30]

The aim of this work is to analyze the evaporation rate of the suspension, which is different from that of the pure solvent in the HVSFS process. The primary objective of this research is to examine the suspension droplet disintegration and evaporation processes inside the HVOF torch. Due to the vaporization of suspension liquid, there is a loss of the HVOF flame enthalpy and kinetic energy; hence, to reduce these losses, a new angular injection technique is applied to increase the efficiency of the present process. Furthermore, the influence of various parameters, such as the nanoparticle concentration and diameter of droplets, on the vaporization rate and on the secondary breakup of the liquid phase and the gas dynamics is discussed in detail. Moreover, this work demonstrates the effectiveness of liquid feedstock usage for nanoparticle injection in the HVSFS process in an industrial diamond jet (DJ2700) torch (Sulzer-Metco, Wohlen, Switzerland).[5,6,23,24,31] This study assumes that the complete evaporation of liquid phase and proper heating and melting of solid nanoparticles is required to obtain a defect-free coating. The improper heating of suspended nanoparticles would lead to a coating comprised of unmelted particles that may result in porous coatings.[21,32]

2. MODEL DESCRIPTION

The model used in this work is the extension of the numerical analysis of the conventional HVOF thermal spray process.[5,6,23,24] The employed turbulent, combustion, discrete phase, flow, and spray models are validated against experimental data and have demonstrated satisfactory pre-

DOI: 10.1021/acs.iecr.5b03956
Ind. Eng. Chem. Res. 2016, 55, 2556−2573

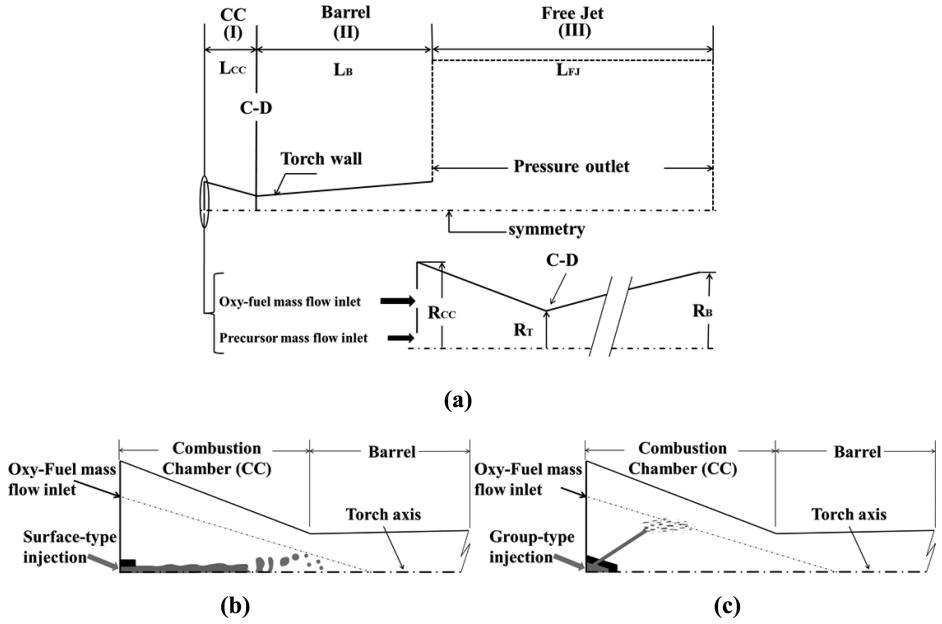

Figure 1. Schematic diagram of the axisymmetric (a) computational domain and boundary conditions, (b) surface-type injection, and (c) group-type injection. In (a) the domain sections are marked as (I) combustion chamber (CC), (II) barrel, and (III) free jet regions, and the vertical line separating the CC and barrel sections is the convergent−divergent (C−D) nozzle throat region.

dictions.[5,6,23,24,31,33−36] For brevity, these model details are not repeated here.

The schematic representation of the computational domain is shown in Figure 1, and the geometric dimensions and working conditions used in the simulations are summarized in Table 1. In all constant diameter cases, the droplet mass flow rate is 1×10^{-4} kg/s, whereas the mass fraction is varied for different diameter droplets in the Rosin−Rammler diameter distribution (see section 2.3). Initial droplet velocities are 15 and 30 m/s (specified based on the diameter of droplets). The injection speed increases to some extent for larger diameter droplets, and it is due to the higher injection force required for larger droplets to penetrate the HVOF jet. Moreover, to inject the particles into the core of the combustion zone, the droplets are added at an angle of 45° and the horizontal and the vertical components of injection velocities are equal to 30 m/s, and from that the mean droplet velocity becomes 42.426 m/s (Table 1). The droplet mass flow rates and velocities are specified based on authors' previous parametric investigations that were aimed to explore optimum operating parameters for the HVSFS spraying process.[5,6,23]

Table 1. Geometric Parameters and Working Conditions for HVSFS Thermal Spray DJ2700 Torch

geometric parameter	symbol	dimension (mm)
(I) combustion chamber length	L_{CC}	23.8
combustion chamber radius	R_{CC}	9.1
nozzle throat radius	R_T	4.2
(II) barrel length	L_B	66.2
barrel exit radius	R_B	6.22
(III) free jet length	L_{FJ}	200
Working Conditions		
oxygen flow rate (kg/s)		0.01197
fuel flow rate (kg/s)		0.003526
droplet constant diameter (μm)		50
droplet flow rate (kg/s)		1×10^{-4}
initial injection mean velocity surface type (ST) (m/s)		15 and 30
initial injection mean velocity group type (GT) (m/s)		42.426
initial temperature (K)		300

First, the numerical model computes the temperature and velocity fields of the HVSFS flame jet in an industrial DJ2700 torch (Sulzer-Metco Wohlen, Switzerland), as depicted in Figure 1. The realizable $k-\varepsilon$ model is used for modeling the turbulence in the jet, including compressibility effects. The thermal and flow fields of the gas are solved by the Eulerian approach. The eddy dissipation model is used to simulate the premixed combustion of oxygen and propane.[37−39]

After complete simulation of the gas phase, ethanol droplets carrying nanoparticles are injected into the HVSFS flame jet, where they undergo several stages. The slow-moving droplets are entrained into the hot flame and are accelerated by the high-velocity gas stream. The first phase is the aerodynamic breakup of droplets.[5,6,23,40] Based on the droplet size and the thermophysical properties their interaction with the surrounding gas is different, and the droplets undergo severe deformation and break up into smaller droplets. The physical breakup process needs to be examined instead of correlating the gas dynamics with droplet fragmentation indirectly to understanding the liquid spraying process.

The secondary breakup of droplets to smaller ones is modeled by the Taylor analogy breakup (TAB) model as the Weber number (We) is lower than 100 ($We < 100$).[23,40] Different regimes of the droplet fragmentation are determined by using the critical value of We. The hydrodynamic force required for the deformation of droplets is related to the surface tension force acting to retain the droplet form by the Weber number ($We = \frac{\rho_c v_{rel}^2 d}{\sigma}$). Since the Ohnesorge number ($Oh = \frac{\mu}{\sqrt{\rho\sigma d}}$) remains much below 0.1 ($Oh \ll 0.1$) in the computational domain, the primary parameter related to the breakup physics is the Weber number. The TAB model is well

DOI: 10.1021/acs.iecr.5b03956
Ind. Eng. Chem. Res. 2016, 55, 2556−2573

Table 2. Thermophysical Properties of Pure Liquid[a] and Suspension[b]

property	mass fraction 0 wt %	5 wt %	15 wt %	25 wt %	temp range (K)
density (kg/m^3)	$\rho_{susp} = aT^3 + bT^2 - cT + d$	$\rho_{susp} = aT^3 + bT^2 - cT + d$	$\rho_{susp} = aT^3 + bT^2 - cT + d$	$\rho_{susp} = aT^3 + bT^2 - cT + d$	250−385
	$a = -3.76345 \times 10^{-6}$	$a = -3.57527 \times 10^{-6}$	$a = -3.1989 \times 10^{-6}$	$a = -2.82258 \times 10^{-6}$	
	$b = 2.27199 \times 10^{-3}$	$b = 2.15839 \times 10^{-3}$	$b = 1.93119 \times 10^{-3}$	$b = 1.70399 \times 10^{-3}$	
	$c = -1.2412$	$c = -1.17914$	$c = -1.05502$	$c = -0.930898$	
	$d = 1053.73$	$d = 1212.55$	$d = 1530.17$	$d = 1847.799$	
viscosity (kg/m·s)	$\mu_{susp} = aT^6 + bT^5 + cT^4 + dT^3 + eT^2 + fT + g$	$\mu_{susp} = aT^6 + bT^5 + cT^4 + dT^3 + eT^2 + fT + g$	$\mu_{susp} = aT^5 + bT^4 + cT^3 + dT^2 + eT + f$	$\mu_{susp} = aT^5 + bT^4 + cT^3 + dT^2 + eT + f$	250−385
	$a = 5.3947 \times 10^{-16}$	$a = 6.13279 \times 10^{-16}$	$a = -1.84601 \times 10^{-13}$	$a = -1.84601 \times 10^{-13}$	
	$b = -1.11875 \times 10^{-12}$	$b = -1.27182 \times 10^{-12}$	$b = 3.19998 \times 10^{-10}$	$b = 3.19998 \times 10^{-10}$	
	$c = 9.6983 \times 10^{-10}$	$c = 1.10252 \times 10^{-9}$	$c = -2.22806 \times 10^{-7}$	$c = -2.22806 \times 10^{-7}$	
	$d = -4.50443 \times 10^{-7}$	$d = -5.12071 \times 10^{-7}$	$d = 7.8043 \times 10^{-7}$	$d = 7.8043 \times 10^{-7}$	
	$e = 1.18439 \times 10^{-4}$	$e = 1.34643 \times 10^{-4}$	$e = -1.37915 \times 10^{-2}$	$e = -1.37915 \times 10^{-2}$	
	$f = -1.67608 \times 10^{-2}$	$f = -1.9054 \times 10^{-2}$	$f = 9.88072 \times 10^{-1}$	$f = 9.88072 \times 10^{-1}$	
	$g = 1.00143$	$g = 1.13845$			
specific heat (J/kg·K)	$c_{susp} = aT^3 + bT^2 - cT + d$	$c_{susp} = aT^3 + bT^2 - cT + d$	$c_{susp} = aT^3 + bT^2 - cT + d$	$c_{susp} = aT^3 + bT^2 - cT + d$	250−385
	$a = 4.42516 \times 10^{-5}$	$a = 4.20390 \times 10^{-5}$	$a = 3.76138 \times 10^{-5}$	$a = 3.3189 \times 10^{-5}$	
	$b = -6.58607 \times 10^{-4}$	$b = -6.25677 \times 10^{-4}$	$b = -5.59816 \times 10^{-4}$	$b = -4.939 \times 10^{-4}$	
	$c = -3.03093$	$c = -2.87938$	$c = -2.57629$	$c = -2.2732$	
	$d = 2227.99$	$d = 2305.59$	$d = 2460.79$	$d = 2616.0$	
thermal conductivity (W/m·K)	$k_{susp} = aT + b$	$k_{susp} = aT^2 + b + c$	$k_{susp} = aT^3 + bT^2 + cT + d$	$k_{susp} = aT^2 + bT + c$	250−385
	$a = -2.640 \times 10^{-4}$	$a = -4.25685 \times 10^{-9}$	$a = -8.21754 \times 10^{-12}$	$a = -1.96341 \times 10^{-7}$	
	$b = 2.468 \times 10^{-1}$	$b = -3.05705 \times 10^{-4}$	$b = -2.95254 \times 10^{-8}$	$b = -6.48697 \times 10^{-4}$	
		$c = 2.89592 \times 10^{-1}$	$c = -4.49135 \times 10^{-4}$	$c = 8.2865 \times 10^{-1}$	
			$d = 4.52780 \times 10^{-1}$		
surface tension (N/m)	$\sigma_{susp} = aT^6 + bT^5 + cT^4 + dT^3 + eT^2 + fT + g$	$\sigma_{susp} = aT^6 + bT^5 + cT^4 + dT^3 + eT^2 + fT + g$	$\sigma_{susp} = aT^6 + bT^5 + cT^4 + dT^3 + eT^2 + fT + g$	$\sigma_{susp} = aT^6 + bT^5 + cT^4 + dT^3 + eT^2 + fT + g$	270−490
	$a = -7.24434 \times 10^{-16}$	$a = -7.24434 \times 10^{-16}$	$a = -7.96877 \times 10^{-16}$	$a = -7.96877 \times 10^{-16}$	
	$b = 1.74074 \times 10^{-12}$	$b = 1.74074 \times 10^{-12}$	$b = 1.91481 \times 10^{-12}$	$b = 1.91481 \times 10^{-12}$	
	$c = -1.7235 \times 10^{-9}$	$c = -1.7235 \times 10^{-9}$	$c = -1.89586 \times 10^{-9}$	$c = -1.89586 \times 10^{-9}$	
	$d = 9.00117 \times 10^{-7}$	$d = 9.00117 \times 10^{-7}$	$d = 9.90129 \times 10^{-7}$	$d = 9.90129 \times 10^{-7}$	
	$e = -2.61702 \times 10^{-4}$	$e = -2.61702 \times 10^{-4}$	$e = -2.87872 \times 10^{-4}$	$e = -2.87872 \times 10^{-4}$	
	$f = 4.01095 \times 10^{-2}$	$f = 4.01095 \times 10^{-2}$	$f = 4.4120 \times 10^{-2}$	$f = 4.4120 \times 10^{-2}$	
	$g = -2.50259$	$g = -2.50259$	$g = -2.75285$	$g = -2.75285$	

[a]Pure liquid properties are taken from *Perry's Chemical Engineering Handbook*[56] and curve-fitted in their temperature range. [b]Suspension properties then are calculated from theoretical models[25,49−51,54,55] in which temperature dependent pure liquid properties are incorporated.

adapted to the conditions of spraying and validated in the earlier studies, found in refs 5, 6, 23, 36, and 40.

The history of suspension droplets is computed with Lagrangian formulation where the finite interphase transport rates and effects of turbulence interactions between the droplet and gas phases are considered.[6,15,16,23,40] By using this treatment, the evaporation history and temperature change for droplets can be calculated during the second stage of heat exchange between the gaseous and liquid phases. The eddy dissipation model is also used to simulate nonpremixed combustion of liquid ethanol drops with remnant oxygen left from premixed (oxygen/propane) combustion.[37−39] The heat and mass transfer of the droplets with the continuous phase is modeled using three laws,[41,42] as described in section 2.1. Finally, the resulting gas flow patterns are defined from the coupled set of equations described in the next section.

The conditions under which each droplet has a set of governing equations are the following:

1. The liquid droplets and the gas phases have their initial continuous velocity and temperature that coexist at each location.

2. The liquid phase has its turbulent fluctuations that result in droplet transport of mass, momentum, and energy. The random effects of turbulence on the particle motion are considered by integrating the individual particle trajectory with the instantaneous fluid velocity.

3. The suspension properties are a function of temperature and are used in the solver by applying nanofluid models, with thermophysical properties of pure liquid and solid particles (Table 2).

Detailed descriptions of the gas phase, discrete phase, droplet breakup, and combustion models are reported elsewhere.[6,23,33−37,43]

2.1. Droplet Heat-Up and Vaporization Model. For modeling heat and mass transfer of the droplet with the continuous phase, three laws, as described below, are used. The inert heating law 1 is applied when the droplet temperature (T_d) is less than the vaporization temperature (T_{vap} = 271 K for liquid ethanol).[6,41,42] A simple heat balance equation (eq 1) is used to relate T_d to the convective heat transfer, and the heat gained or lost by the droplet while moving through the continuous phase.

Law 1:

DOI: 10.1021/acs.iecr.5b03956
Ind. Eng. Chem. Res. 2016, 55, 2556−2573

for $T_d < T_{vap}$,

$$m_d c_d \frac{dT_d}{dt} = hA_d(T_\infty - T_d) \quad (1)$$

where m_d, c_d, T_d, and A_d are the mass, heat capacity, temperature, and surface area of the droplet, respectively. Here, h and T_∞ are the convective heat transfer coefficient and gas temperature.

The mass transfer law 2 is applied to predict the vaporization from a discrete phase droplet using eq 2. This law is used when droplet temperature reaches T_{vap} and continues until the droplet reaches the boiling point.

Law 2:

for $T_{vap} < T_d < T_{boil}$,

$$N_i = k_c(C_{i,s} - C_{i,\infty}) \quad (2)$$

where N_i, k_c, $C_{i,s}$, and $C_{i,\infty}$ are the molar flux of vapor, mass transfer coefficient, vapor concentration at the droplet surface, and vapor concentration in the bulk gas, respectively. k_c in eq 2 is calculated from the Sherwood number (Sh) correlation.[44,45]

The droplet mass is reduced according to eq 3:

$$m_d(t + \Delta t) = m_d(t) - N_i A_d M_w \Delta t \quad (3)$$

where M_w is the molecular weight of species i. During the activation of law 2, the droplet temperature is updated using the heat balance eq 4. It relates the sensible heat change in the droplet to the convective and latent heat transfer between the droplet and the continuous phase.

$$m_d c_d \frac{dT_d}{dt} = hA_d(T_\infty - T_d) + \frac{dm_d}{dt} L \quad (4)$$

here dm_d/dt is the rate of evaporation and L is the latent heat.

For predicting the convective boiling of droplets, law 3 is applied. It uses the boiling rate eq 5 and is activated when droplets reach the boiling point (T_{boil} = 351 K for liquid ethanol).[6,37]

Law 3:

for $T_d \geq T_{boil}$,

$$\frac{d(d_d)}{dt} = \frac{4K_\infty}{\rho_d c_\infty d_d}(1 + 0.23\sqrt{Re_d}) \ln\left[1 + \frac{c_\infty(T_\infty - T_d)}{L}\right] \quad (5)$$

where K_∞ and c_∞ are the thermal conductivity and the heat capacity of the gas, and ρ_d is the droplet density.

The droplet with an injection temperature of 300 K enters the hot CC for gradual evaporation and combustion with remnant oxygen left after premixed propane/oxygen burning. Since the Knudsen number ($Kn = \lambda/d_d$, the ratio of the gas mean free path λ to the droplet diameter d_d) is far less than the transition number 0.01, the discontinuous effects are neglected.[46,47] It is also stated that the dependence of the drag coefficient (C_D) on Kn can be neglected in the case of HVOF spraying.[48] The Reynolds number (Re) varies from 2.09 × 10^5 to 1.18 × 10^5 in the computation domain based on the characteristics of the gas dynamics.

2.2. Nanoparticle Suspension Theoretical Model. The thermophysical and transport properties of nanoparticles are quite different from those of their original solid substance (in bulk).[25] The necessary thermophysical properties of nanoparticle suspension are calculated from the nanofluid model, as described below. The density of nanofluids is determined by using the mixture rule (eq 6)[49]

$$\rho_{susp} = (1 - C)\rho_l + C\rho_p \quad (6)$$

where C is the volume concentration of solid particles in suspension, ρ_l is the density of liquid ethanol, and ρ_p is the density of solid titania particles with a value of 4230 kg/m^3. The value of the suspension density ρ_{susp} increases by the increment in percentage concentrations of nanoparticles from 0 to 25 wt %. The analysis shows that an increase in temperature will gradually decrease the overall value of suspension density because of reduction in the base fluid density (Table 2).

For the viscosity of a suspension (μ_{susp}), Einstein's formula is restricted to the low volume concentration {$\mu_{susp} = \mu_l(1 + 2.5C)$} and it is modified by Brinkman for a higher concentration of nanoparticles (eq 7)[25,50] as under

$$\mu_{susp} = \frac{\mu_l}{(1 - C)^{2.5}} \quad (7)$$

where μ_l is the viscosity of liquid ethanol. The consequence of temperature variation on the viscosity of the suspension is similar to that of the density; i.e., a gradual increase in temperature will decrease the viscosity (Table 2).[28]

The specific heat also increases with increasing the percentage concentration of nanoparticles in the suspension; furthermore, it has a direct relation to temperature increment[25,51] (Table 2).

$$c_{susp} = Cc_p + (1 - C)c_l \quad (8)$$

where c_p is the specific heat capacity of titania powder (3780 J/kg·K), and c_l is the specific heat capacity of liquid ethanol.

From experimental work, researchers prove that thermal conductivity (k_{susp}) of nanofluids increases with the increment of nanoparticle concentration; however, it also depends on the size, shape, and temperature of suspended particles.[28,52,53] For thermal conductivity of spherical nanoparticles, the Bruggeman model gives better predictions[51,54,55] than other models with no limitation on the volume concentration of solid particles in suspension.

$$k_{susp} = \frac{1}{4}[(3C - 1)k_p + (2 - 3C)k_l] + \frac{k_l}{4}\sqrt{\Delta} \quad (9)$$

$$\Delta = (3C - 1)^2\left(\frac{k_p}{k_l}\right)^2 + (2 - 3C)^2 + 2(2 + 9C + 9C^2)\left(\frac{k_p}{k_l}\right) \quad (10)$$

where k_p is the thermal conductivity of titania powder (k_p = 10.4W/m·K) and k_l is the thermal conductivity of the base fluid.

It is reported that the surface tension of ethanol based suspension does not deviate much from that of the pure ethanol for low particle concentrations (up to 3 wt %),[25,52] after which the surface tension increases with increasing nanoparticle concentration.[27,28] A 10% increase is noticed for a nanoparticle concentration of 10 wt %. It is because of the rise in the van der Waals forces between nanoparticles at the interface between the liquid and gas, which causes an increase in surface tension. Furthermore, the latent heat of vaporization has a direct relation to the cohesive forces. Hence, the rise in surface

DOI: 10.1021/acs.iecr.5b03956
Ind. Eng. Chem. Res. 2016, 55, 2556−2573

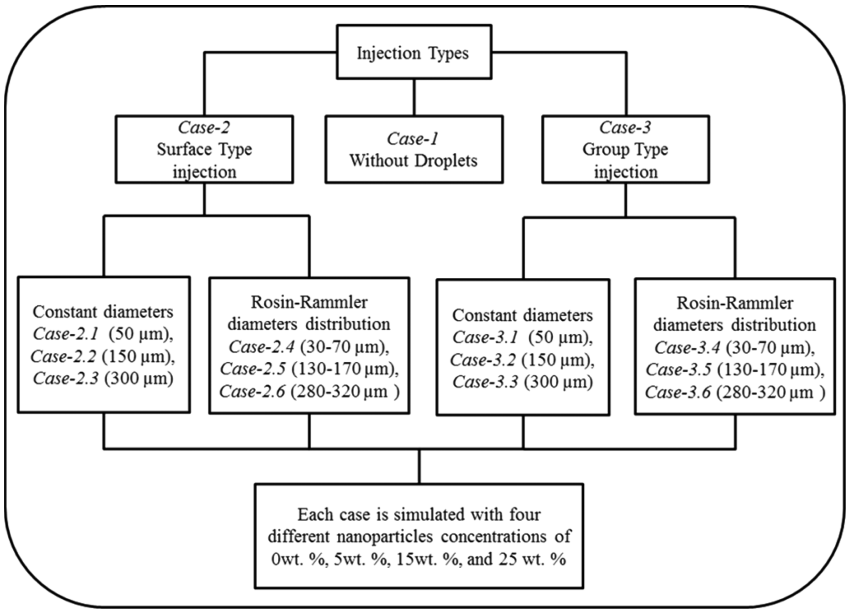

Figure 2. Droplet injection types and case division.

tension increases the value of heat required to evaporate the base liquid carrying nanoparticles.[29]

In this work, four different solid nanoparticle concentrations (0, 5, 15, and 25 wt %) suspended in pure ethanol are studied. The surface tension of the suspension is calculated by 10% increase for two concentrations of 15 and 25 wt % (eq 11):

$$\sigma_{15,25\%\,\mathrm{susp}} = \sigma_{0\%\,\mathrm{susp}} + (10\%(\sigma_{0\%\,\mathrm{susp}})) \tag{11}$$

It should be noted that nonhomogeneous effects of suspended nanoparticles (titania) in the solvent (ethanol) are considered in the numerical modeling of droplet flow inside the torch. The solid powders are not charged into droplets, as the primary aim of this work is to track the effect of solid loading on droplet breakup and evaporation numerically. The addition of nanoparticles in the suspension is incorporated by modifying pure liquid properties using the correlations mentioned in eqs 6−11. The suspension properties are calculated from commonly used theoretical models.[25,50−52,54,55] The temperature dependent pure liquid properties are calculated by a curve-fitted procedure in the required temperature range as shown in Table 2.[56]

2.3. Droplet Injection Properties. Many cases are solved by analyzing different injection schemes related to the droplets' atomization in the CC of the thermal spray gun. A detailed picture can be seen in Figure 2 for the cases considered. Here, "without droplets" (case 1) in Figure 2 refers to a case in which droplets are not injected, and only combustion gas flow characteristics in HVSFS process are analyzed. The two main injection schemes of surface type (ST, case 2) and group type (GT, case 3) are employed to see the effects of varied injection types on gas dynamics and droplet dynamics. In the surface-type (ST) injection method, streams of droplets are released axially (at an angle of 0° with the horizontal axis) from each facet of the surface. As the droplets move along the axis, the solver simulates the interaction of droplets with the combustion gas along the central axis of the torch. For group-type (GT) injection, droplets are injected at an angle of 45° into the core of the combustion zone. For these two injection types, different sizes of droplets with constant and Rosin−Rammler diameter distributions are considered. First, torch flow dynamics are studied for constant diameter droplets of 50, 150, and 300 μm having nanoparticle concentrations of 0, 5, 15, and 25 wt %. In the second type, a similar study is repeated for Rosin−Rammler diameter distribution of droplets having size variations of 30−70, 130−170, and 280−320 μm (Figure 2).

The Rosin−Rammler diameter distribution is applied that allows the range of diameters divided into an adequate number of discrete intervals. The Rosin−Rammler distribution function is based on the assumption that an exponential relationship exists between the droplet diameter, d, and the mass fraction of droplets with a diameter greater than d and is given as[57−59]

$$Y_d = e^{-(d/\bar{d})^n} \tag{12}$$

where $\bar{d}$ is the size constant (mean diameter), and n is the size distribution parameter (spread parameter). The mass fraction of these droplets is dependent on diameter. The mass fraction of larger diameter droplets is lower than that of the smaller diameter droplets (Table 3). Table 3 shows the Rosin−Rammler diameter distribution with different mass fractions of the suspension droplets.

Table 3. Rosin−Rammler Diameter Distribution with Different Mass Fractions

diam (μm)	mass fraction	diam (μm)	mass fraction	diam (μm)	mass fraction
30	0.844	130	0.548	280	0.461
40	0.631	140	0.457	290	0.414
50	0.368	150	0.368	300	0.368
60	0.152	160	0.284	310	0.323
70	0.040	170	0.210	320	0.280

For each type of droplet injection, different rates of evaporation and fragmentation have been detected. Also, the effect of droplet breakup and evaporation on gas dynamics is changed with varying injection parameters (Figure 2). It is due to the variation in droplet interaction with the continuous combustion gas inside the HVSFS torch. Results and

DOI: 10.1021/acs.iecr.5b03956
Ind. Eng. Chem. Res. 2016, 55, 2556−2573

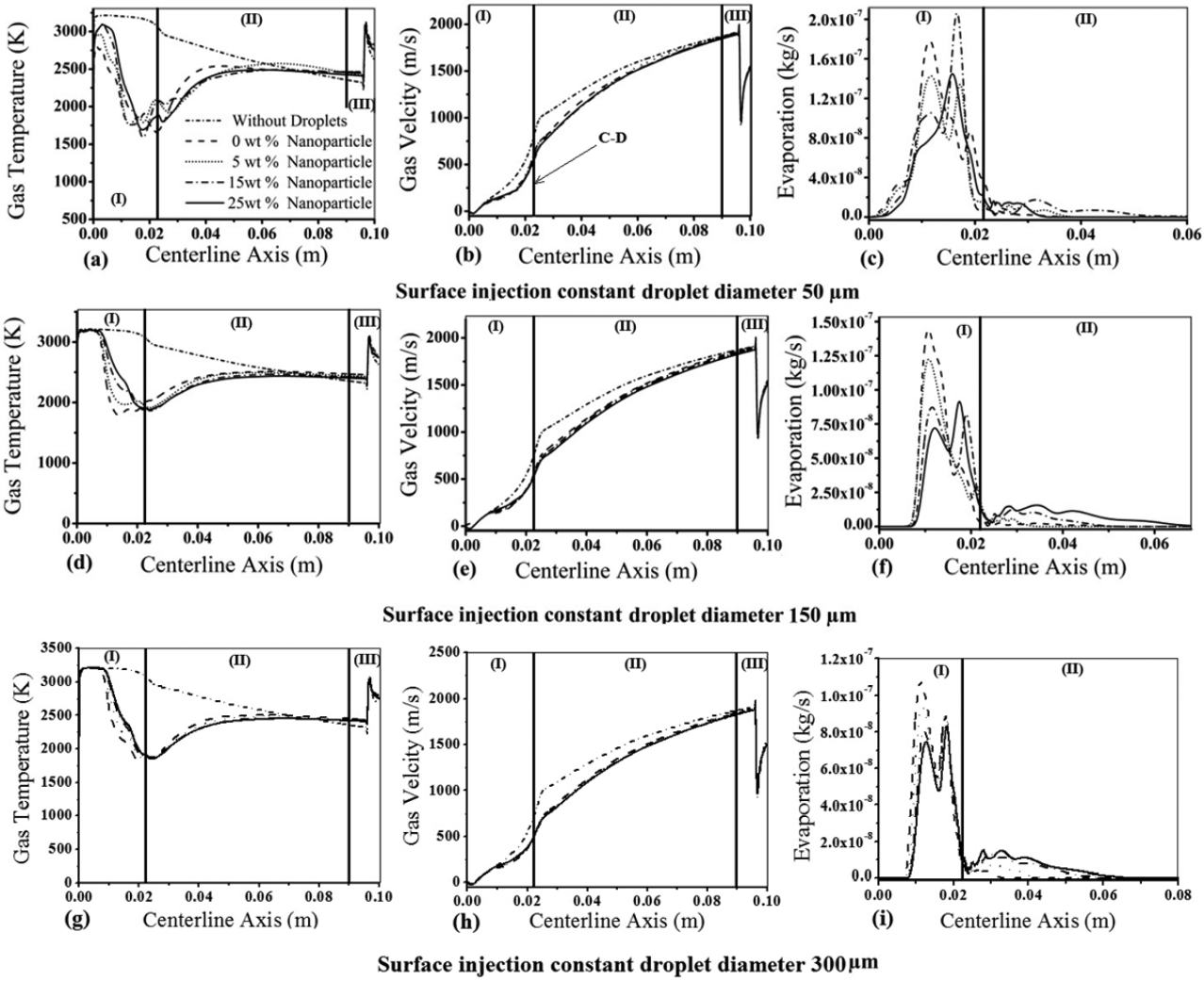

Figure 3. Comparison of gas temperature, velocity field, and rate of evaporation experienced by droplets injected from the surface with constant diameters of (a–c) 50, (d–f) 150, and (g–i) 300 μm, having different solid nanoparticle concentrations. In all figures the domain sections are marked as (I) combustion chamber (CC), (II) barrel, and (III) free jet regions, and the vertical line separating the CC and the barrel sections is the convergent–divergent (C–D) nozzle throat region.

Discussion addresses how gas dynamics, the rate of evaporation, and secondary breakup of liquid drops are influenced by varying the concentration of solid nanoparticles in the liquid feedstock droplets. In the results, "without droplets" (case 1) refers to a case in which only combustion gas flow characteristics in the HVSFS process are analyzed. Moreover, the domain sections in the figures are marked as (I) combustion chamber (CC), (II) barrel, and (III) free jet, respectively (see Figure 1, Table 1). Furthermore, the vertical line separating the CC and the barrel sections is the convergent–divergent (C–D) nozzle throat region. These section names are used to explain the gas dynamics and the droplet dynamics in different areas of the torch. Likewise, for a clear understanding, the effects of varied nanoparticle loading with varied injection parameters on the gas dynamics and the droplet secondary breakup are presented as different sections. It may be noted that for brevity, not all cases mentioned in Figure 2 are discussed in detail; however, the main analysis is included.

3. RESULTS AND DISCUSSION

3.1. Effects of Nanoparticle Suspension on the Gas Dynamics and the Rate of Droplet Vaporization in HVSFS Process.

3.1.1. Surface-Type (ST) Injection. The first set of simulations is performed for axial injection of droplets from a centralized inlet surface into the torch. This injection type is used for injecting (A) constant diameter droplets and (B) varied diameter droplets. For each case four nanoparticle concentration loadings are used: 0, 5, 15, and 25 wt %. The effects of increasing nanoparticle loading inside the liquid feedstock on torch's flow dynamics, and droplets' rate of evaporation are discussed in sections 3.1.1.1 and 3.1.1.2.

3.1.1.1. Constant Diameter Droplet Injection. Case 2.1 is simulated for analyzing injection of droplets from the surface having a constant diameter of 50 μm, with a velocity of 15 m/s, and a mass flow rate of 1×10^{-4} kg/s, using different solid nanoparticle concentrations (Table 1). When these droplets are added to the gun, cooling effects are detected over the hot gas near the CC back wall as compared to the without droplet case (case 1) (Figure 3a). The temperature drop noticed for two extreme nanoparticle concentrations, 0 and 25 wt %, is 440 and 120 K, respectively (at x = 0.0033 m from the point of injection, Figure 3a). Moreover, the gases experience more cooling after the C–D nozzle for drops having a high concentration of 25 wt % with a temperature difference of

DOI: 10.1021/acs.iecr.5b03956
Ind. Eng. Chem. Res. 2016, 55, 2556–2573

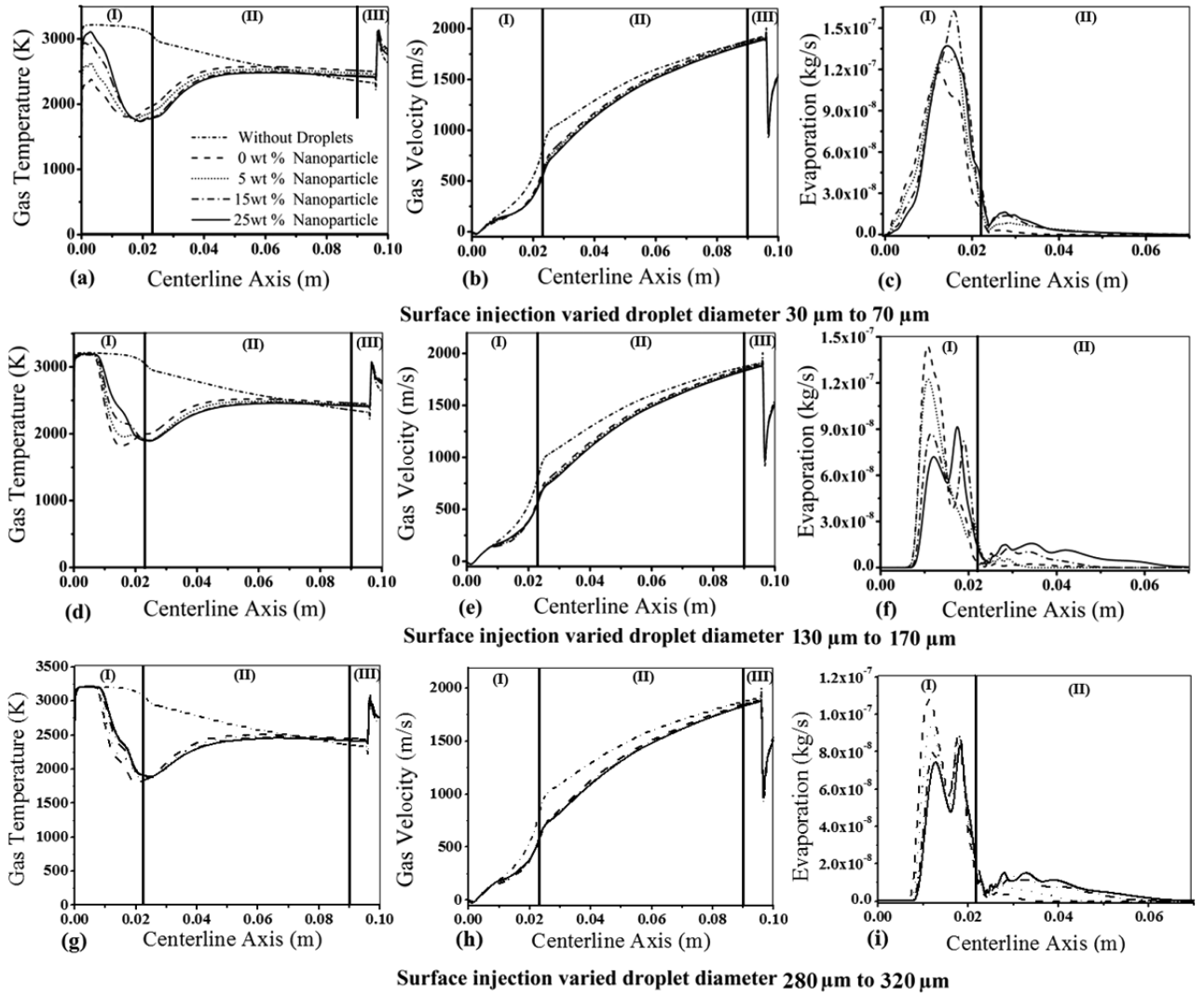

Figure 4. Comparison of gas temperature, gas velocity field, and rate of evaporation experienced by droplets injected from the surface with varied diameters of (a–c) 30, 40, 50, 60, and 70 μm; (d–f) 130, 140, 150, 160, and 170 μm; and (g–i) 280, 290, 300, 310, and 320 μm, having different solid nanoparticle concentrations.

390 K as compared to 250 K for 0 wt % droplets (at x = 0.04042 m from the point of injection, Figure 3a). It is also reflected in the velocity field of the HVSFS process, where the variation in velocity is 114 m/s between the without droplet case , case 1, and the case with 0 wt % nanoparticle concentration droplet injection (at x = 0.04042 m from the point of injection, Figure 3b). This difference increases to 161 m/s when compared to the case of 25 wt % nanoparticle concentration (Figure 3b). It can be seen that lower velocities are predicted for the high-concentration droplets. The reason can be the cooling of the combustion gas that leads to the small pressure drop that causes some decrement in the velocity. However, the difference in gas velocities for different nanoparticle concentrations is not very significant.

The rate of evaporation of droplets with different solid nanoparticle concentrations is compared in Figure 3c. The result shows that temperature fluctuations in the HVSFS process are a direct function of the energy required for droplet vaporization. In particular, less cooling of gas is observed with lower heat requirement for evaporation and vice versa. The highest value of the rate of evaporation is detected for homogeneous droplets (1.83×10^{-7} kg/s for 0 wt % nanoparticle loading). With adding 25 wt % nanoparticles into the base fluid, the rate of evaporation is reduced by 20%. Downstream of the C–D nozzle, higher cooling and vaporization rates are identified for high concentration droplets. The maximum rate of evaporation occurs inside the CC for all droplets, while the final location of evaporation stretches to the gun exit when droplets are loaded with higher concentrations. It proves that heat of vaporization required for the non-homogenous droplets is much greater than that required for the homogeneous droplets. The overall data show that pure ethanol droplets are entirely vaporized in the CC section, resulting in the highest gas cooling and temperature drop in section I. Solid-loaded drops are not completely vaporized, resulting in less gas cooling in the CC, but somewhat greater cooling in the expansion nozzle where vaporization continues. The reason for this heat imbalance is obviously due to an increase in the heat capacity of the high concentration droplets that take longer to reach the boiling point, which, in turn, delays the evaporation process. It was stated in section 2.2 that the specific heat of suspension droplets increases with increasing the percentage concentration of nanoparticles in the suspension. Thus, the heat required to raise the

DOI: 10.1021/acs.iecr.5b03956
Ind. Eng. Chem. Res. 2016, 55, 2556–2573

temperature of the highly concentrated suspension droplets is much higher than that for less concentrated or 0 wt % suspension droplets. Hence, more cooling is observed in the barrel for higher concentration suspension cases.

In case 2.2 droplets are injected with the mass flow rate, velocity, and constant diameter of 1×10^{-4} kg/s, 30 m/s, and 150 μm, respectively. A comparison of the variation in HVSFS process temperatures, velocities, and rate of evaporation experienced by these droplets along the centerline is shown in Figure 3d–f. First cooling is detected before the C–D nozzle with a temperature difference of about 730 K between two extreme cases (droplets with highest and lowest concentration, i.e., 25 and 0 wt %). It is much larger than the 390 K temperature difference as observed in the case of droplets injected with 50 μm diameter (case 2.1). It confirms that larger size droplets cause more cooling inside the HVSFS torch. The second most significant temperature difference in case 2.2 is just after the C–D nozzle, and it is about 150 K. It reduces to 85 K in the middle of the barrel and reaches a negligible value at the gun exit (Figure 3d).

The velocity field in the case 2.2 experiences small changes as solid particles are loaded with a droplet size of 150 μm, and this difference reaches 45 m/s just after the C–D nozzle (Figure 3e). Moreover, a significant difference in the evaporation of droplets with different concentrations is noticed inside the CC. The highest and the lowest evaporation rates of 1.54×10^{-7} kg/s and 9.52×10^{-8} kg/s are observed for drops with 0 and 25 wt % concentration loadings, respectively. When these values of case 2.2 are compared with those of case 2.1, a 15% decrease in evaporation is noticed, which suggests that the increasing size of the injection droplet could reduce the vaporization of the liquid feedstock.

In contrast, as the droplet diameter is further increased to 300 μm (case 2.3), the maximum gas temperature difference along the centerline between two cases (0 and 25 wt %) reaches 460 K in the CC (Figure 3g). In the barrel, it remains below 100 K, and at the gun exit, the temperature difference between all nanoparticle concentrations is negligible. The velocity variations for different concentrations are not considerable (Figure 3h). A similar trend is observed in the droplet vaporization rate compared to the earlier analysis (case 2.2 with 150 μm droplet size) and the difference in the rate of evaporation for different nanoparticle loadings is further reduced (Figure 3i). It is seen in Figure 3f,i that the droplet evaporation is delayed for the bigger diameter droplets and they start evaporating at $x = 0.00747$ m from the point of injection. The smaller diameter droplets (50 μm) start evaporating immediately after injection into the CC (see Figure 3c). First, there is a reduction in the diameter of 150 and 300 μm droplets and an increase in Weber number, and droplet deformation and atomization are observed inside the torch CC (see section 3.2.1 for details of droplet fragmentation). After some deformations, these droplets start evaporating. Hence, an overall delay in the evaporation is observed for the large diameter droplets.

3.1.1.2. Varied Diameter Droplet Injection. The effect of injecting different diameter droplets from a surface is studied by using three sets of Rosin–Rammler diameter distributions, as mentioned in Figure 2. In case 2.4, five streams with varied diameters of 30, 40, 50, 60, and 70 μm are injected at the same time from a surface having a Rosin–Rammler diameter distribution (Figure 4a). For these droplet injections the difference in temperature between without droplets (case 1) and droplets with nanoparticles (case 2.4) increases. For high nanoparticle loading (25 wt %) the temperature difference is 145 K, while in low nanoparticle loading (e.g., 0 wt %) it is 850 K. The result shows an increase in temperature drop for low nanoparticle loading in comparison to case 2.1. Hence, it confirms that more evaporation occurs for varied diameter drops than for the constant diameter drops. After the C–D nozzle massive evaporation of droplets with the high concentration of nanoparticles (25 wt %) affected the gas temperature difference and increased it up to 370 K, while for 0 wt % nanoparticle loading it is 250 K. This increase in temperature difference for varied diameter drops injection depicts that the rate of vaporization is dependent on the droplet injection diameter. For small diameter drops (30, 40 μm) evaporation occurs mainly inside the CC, while larger diameter drops (60, 70 μm) get evaporated in the barrel.

Compared to the value of velocity in case 2.1, when five differently sized droplet streams are added, the effect on gas velocity intensifies (Figure 4b). For 0 wt % concentration, the velocity difference between case 2.1 (with constant diameter droplets) and case 2.4 (with varied diameter droplets) becomes 165 m/s, while for 25 wt % loading the difference observed is 220 m/s (Figure 4b). This increment in velocity difference is due to the higher cooling effect and the presence of droplets of varying size from 30 to 70 μm. In this case, every drop has a different evaporation rate and is moving with a different velocity inside the torch. Hence, these changing drops' velocities have different rates of interaction with the combustion gases, which results in larger variations in the gas dynamics as compared to constant diameter droplets.

The rates of evaporation of varied diameter droplets for different solid concentrations are presented in Figure 4c. It illustrates that 0 wt % drops have a lower evaporation rate (1.2×10^{-7} kg/s) in comparison to 25 wt % (1.36×10^{-7} kg/s) droplets along the centerline axis. Nevertheless, the overall evaporation rate inside the CC is higher for 0 wt % loaded drops in comparison to that of 25 wt % loaded drops. The variation in the rate of evaporation is because of the difference in the diameters of droplets that have different mass fractions (Table 3). Small drops ($d \leq 50$ μm) carry high mass fractions, but due to the smaller size, the evaporation started earlier and completed at a much faster rate than the larger droplets. By contrast, the large diameter droplets ($d > 50$ μm) have lower mass fractions, and they experience high aerodynamic forces that first lead to the disintegration of the droplets, and then their evaporation occurs. Hence, for larger droplets a delay in their evaporation process is observed due to the requirement of a huge amount of heat to bring the larger droplets to their point of evaporation. Also, a 10-fold increase in the diameter of droplets implies a 1000-fold rise in the volume, and hence in the heat capacity. Therefore, the drops can absorb a large amount of heat without being vaporized, at least in the first instant, before the breakup begins. Additionally, the increase in nanoparticle concentration also affects the vaporization of these different diameter droplets, and high concentration drops show decreased levels of evaporation due to a further increase in the heat capacity (as explained in section 2.2, Table 2).

Similarly, when droplets are injected with the mass flow rate of 1×10^{-4} kg/s, the velocity of 30 m/s, and different diameters of 130, 140, 150, 160, and 170 μm, the trends for gas temperature cooling are changed. Moreover, the gas velocity decreases, and reduced evaporation rates for droplets are observed (case 2.5). Here, the temperature difference in the middle of the CC between 0 and 25 wt % nanoparticle loading

DOI: 10.1021/acs.iecr.5b03956
Ind. Eng. Chem. Res. 2016, 55, 2556–2573

is 550 K, and it decreases to 100 K along the barrel central axis (Figure 4d). In Figure 4e the velocity field does not experience any significant change and shows the same difference as observed for case 2.2 with constant diameter 150 μm drop injection. It is because the mean diameter of the Rosin−Rammler distribution is 150 μm and this droplet size carries the high mass fractions of a liquid feedstock as compared to the other size droplets.

In Figure 4f, vaporization detected in case 2.5 is 1.40×10^{-7} and 7.67×10^{-7} kg/s for 0 and 25 wt % nanoloading, respectively. Furthermore, an analysis of case 2.5 shows a decrease in the overall evaporation along the gun axis by 9% for 0 wt % loading and by 19% for 25 wt % loading when compared to case 2.2. It is because the large droplets initially absorb a huge amount of heat without evaporation, and start vaporizing once fragmentation has reduced their size significantly. The final location of droplet evaporation moves from the C−D nozzle toward the middle of the barrel for 0 and 5 wt % nanoparticle concentrations. The droplets with 15 and 25 wt % nanoparticle concentrations leave the HVSFS torch without complete evaporation, and they are ejected out into the atmosphere. As more concentrated droplets have a higher surface tension, and they require more heat to vaporize, their evaporation process is also delayed. In case 2.6, when the set of droplet diameters of 280, 290, 300, 310, and 320 μm are injected, no significant variations are observed as compared to the constant diameter (300 μm) case 2.3. It confirms that all these drops have similar trends of gas cooling, gas velocity, and rate of evaporation (Figure 4g−i).

In summary, for surface-type injection, the effect on drop evaporation is dependent on two parameters, i.e., an increase in the nanoparticle concentration and an increase in droplet diameter. As the drop size and nanoparticle concentration increase, the rate of evaporation decreases. For ST injection, the varied diameter set of 30−70 μm increases the rate of evaporation in comparison to constant 50 μm diameter. Moreover, for the second and third sets of varied diameters of 130−170 and 280−320 μm, the effect is reversed due to increased droplet sizes. It is concluded that the increasing nanoparticle concentration in liquid feedstock droplets with varied large sizes would decrease the droplet evaporation process. For many practical applications, injected drops have different diameters and the trend of change in gas temperature, velocity, and drop evaporation is very similar to that illustrated in this section.

3.1.2. Group-Type (GT) Injection. Similar to ST injection, the GT injection uses two streams having (A) constant diameter droplets and (B) varied diameter droplets (see Figure 2). The GT injection is not axial, and its direction is set at an angle of 45° (with the horizontal axis). This is to increase the interaction time of suspension droplets with higher temperature gases, and to reduce the evaporation length of ethanol droplets and to confine the evaporation within the CC and the barrel sections of the HVSFS torch.[15,16] All cases are simulated for four different nanoparticle concentrations of 0, 5, 15, and 25 wt %. For brevity, the results related to GT injections are presented only for 150 μm (constant diameter) and 130−170 μm diameter droplets (Rosin−Rammler diameter distributions). The results are presented in sections 3.1.2.1 and 3.1.2.2.

3.1.2.1. Constant Diameter Droplet Injection. In case 3.2, the droplets are injected in the form of a group with the angle of injection of 45° to observe the effects over the gases inside the torch's combustion chamber (CC) and in the barrel section II. These drops are not moving along the centerline axis of the gun. The droplets are injected with the mass flow rate of 1×10^{-4} kg/s, the velocity of 42.426 m/s, and a constant diameter of 150 μm into the HVSFS torch. These droplets influence the centerline temperature and the velocity of gases when they converge on the torch central axis after striking the CC walls (Figure 5). In the previous case 2.2 with ST injection, the angle

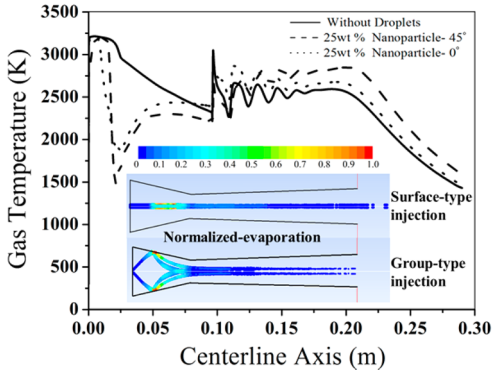

Figure 5. Comparison of gas temperature and normalized droplet evaporation with surface-type injection (angle of injection 0°) and group-type injection (angle of injection 45°) of constant diameter droplet of 150 μm and having 25 wt % nanoparticle concentrations.

of injection is 0°, and the droplets move along the centerline axis of the torch, while in the GT injection the angle of injection is varied and the droplets move at 45° angle with the torch's centerline axis (Figure 5). Therefore, the droplets are injected into the core of the combustion zone, and come in direct contact with the hot flame. They reach the evaporation point rapidly in comparison to the ST injection case 2.2 and evaporate completely within the torch. Furthermore, it can be seen in Figure 5 that, due to the complete evaporation of droplets inside the torch, the temperature of the flame increases in the free jet region of the GT injection case. However, it is observed that greater gas cooling occurred for the GT injection; the reason is that GT injection supports higher evaporation of droplets, and the rate of evaporation is increased up to 67%. As droplets come in direct contact with the combustion gases in the hottest zones of CC, they receive more thermal energy to heat the suspension and suspended nanoparticles.

The effect of droplet evaporation on the centerline temperature and velocity for case 3.2 is also shown in Figure 6a,b. When droplets converge along the centerline axis after striking the CC walls, they start to influence the gas dynamics along the x-axis. Only the droplets with 25 wt % concentration are converged along the central axis, while others evaporated in the vicinity of the combustion zone. The temperature reduction before the C−D nozzle is about 1400 K for droplets with 25 wt % concentration in contrast to the without droplets case 1, and downstream of the C−D nozzle it becomes 900 K. Other drops carrying 0, 5, and 15 wt % nanoparticles get evaporated in the CC as they come in direct contact with the flame and leave the nanoparticles that accelerate and get heated in the nozzle and the barrel sections.

Similarly, the velocity field of combustion gases along the axis is influenced by the droplets carrying 25 wt % nanoparticle concentration, and the difference is about 220 m/s. Furthermore, the rates of evaporation of droplet streams are captured along their actual path in the direction of increasing x-position, as shown in Figure 6c. It can be seen that drops with

DOI: 10.1021/acs.iecr.5b03956
Ind. Eng. Chem. Res. 2016, 55, 2556−2573

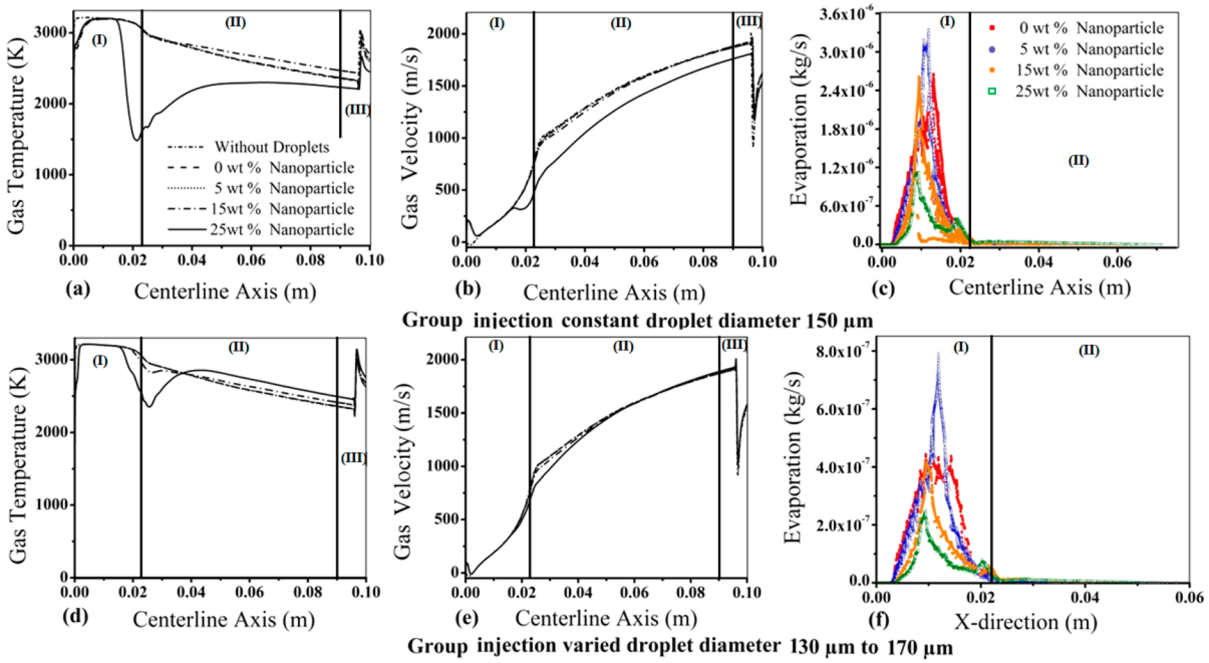

Figure 6. Comparison of gas temperature, gas velocity field, and rate of evaporation experienced by droplets injected as a group at an angle of injection of 45° with constant diameter (a–c) 150 μm and with varied diameters of (d–f) 130, 140, 150, 160, and 170 μm, having 0, 5, 15, and 25 wt % nanoparticle concentrations.

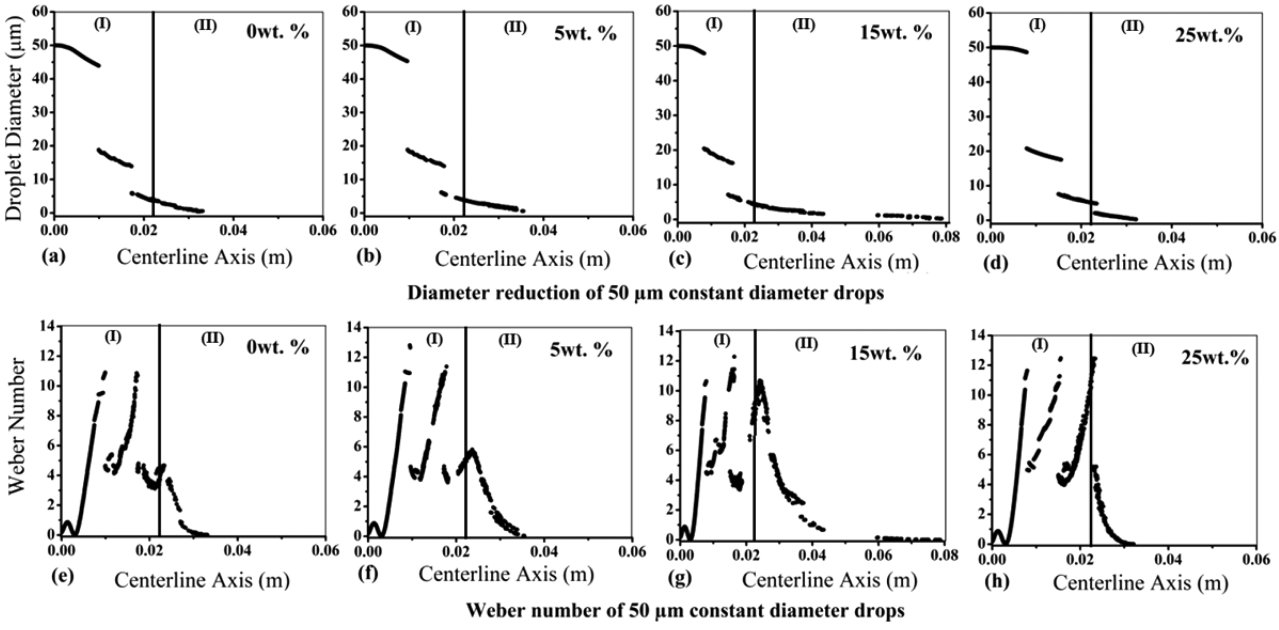

Figure 7. Comparison of (a–d) droplet diameter reduction and (e–h) Weber number for surface-type injection with a constant diameter of 50 μm having 0, 5, 15, and 25 wt % nanoparticle concentrations.

0, 5, and 15 wt % concentrations have values of their peak evaporation rate of 2.59×10^{-6}, 3.30×10^{-6}, and 2.62×10^{-6} kg/s, respectively, in the middle of the CC. To the contrary, droplets with 25 wt % concentration have the lowest evaporation rate of 1.11×10^{-6} kg/s. It is also shown that for the GT injection the evaporation is lower when the droplets carry a higher percentage of nanoparticle concentration. However, these rates of evaporation are considerably higher than the ST injection case 2.2; overall the increment in vaporization is 94 and 91% for 0 and 25 wt % nanoloading, respectively.

3.1.2.2. Varied Diameter Droplet Injection. The droplets with varied diameters of 130, 140, 150, 160, and 170 μm are injected into the core of the combustion zone (case 3.5), and the results for gas temperature and velocity along the central axis are presented in Figure 6d,e. Except for 25 wt % loading, no considerable change is evident in the centerline temperature and velocity profiles as varied diameter drops move away from the central axis. For 25 wt % loading there is a significant difference as compared to case 1, although it is much lower than case 3.2 (Figure 6a,d).

DOI: 10.1021/acs.iecr.5b03956
Ind. Eng. Chem. Res. 2016, 55, 2556–2573

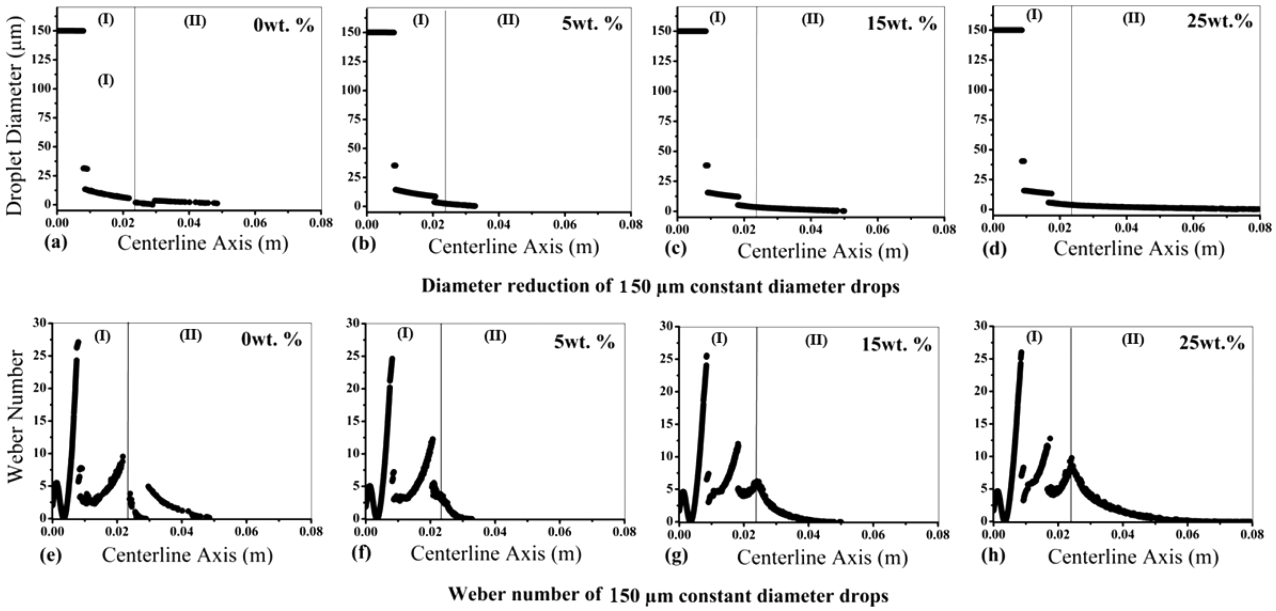

Figure 8. Comparison of (a–d) droplet diameter reduction and (e–h) Weber number for surface-type injection with a constant diameter of 150 μm having 0, 5, 15, and 25 wt % nanoparticle concentrations.

When differently sized diameters in GT injection (case 3.2) are compared to constant size GT injection (case 3.5), significant reduction in the rate of evaporation is observed for all concentrations of nanoparticles (Figure 6c,f). For 0 and 25 wt % nanoparticle loadings the reduction in evaporation is about 83 and 78%, respectively. These variations are the result of greater fragmentation of larger droplets, the difference in the relative velocities of droplets, and the requirement of high heat of vaporization, which in turn reduces the evaporation process. The behavior of other GT injections with the constant diameters of 50 and 300 μm, and with variable drop sizes of 30–70 and 280–310 μm is more or less similar, and for conciseness figures of these results are not included.

It is observed that when suspension droplets are fed into the HVSFS by using the surface-type injection at a 0° angle of injection, the gas enthalpy and kinetic energy are decreased, and accordingly the efficiency of the HVSFS flame is reduced significantly (as shown in Figure 5). To reduce this cooling effect and to add more energy to the HVSFS flame, GT injection is carefully chosen, and it works efficiently. The overall behavior of the GT injection is more efficient than the ST injection as low gas cooling is observed along the centerline axis and a high rate of droplet evaporation is noticed inside the CC. Hence, it can improve the solid particle heating, and improved kinetic energies can generate denser coatings.

3.2. Effects on Secondary Breakup. The TAB model captured the droplet secondary breakup, and the Weber number (*We*) detected in all cases remains below 100. Since droplet fragmentation in the HVSFS process is one of the major physical phenomena, a thorough investigation on breakup is carried out in all cases. For the analysis, droplet streams with constant diameter injected in the gun are picked up, and results in diameter reduction and final location of evaporation are highlighted. Furthermore, for the Rosin–Rammler diameter distribution, a set of five streams are analyzed for clarity. Since in all the cases the droplet Ohnesorge number (*Oh*) remains below 0.1, *We* is the dominating parameter that is analyzed here in detail.[23,40]

3.2.1. Surface-Type Injection. 3.2.1.1. Constant Diameter Droplet Injection. A comparison of droplet diameter reduction is shown in Figure 7a–d for ST injection (case 2.1). It demonstrates the secondary breakup and a decrease in the diameter of 50 μm droplets with four different solid nanoparticle concentrations. It can be seen that droplets experience a sharp decrease in diameter from 45 to 20 μm and from 20 to 10 μm approximately for all nanoparticle concentrations.

Comparison of *We* variations for droplets in the computational domain is depicted in Figure 7e–h. In case 2.1, *We* reached a peak value of about 12 in the CC where the main atomization occurs due to relative velocities between the droplets and the gas phase in the CC. However, the value of *We* remains below 14 for all nanoloadings; hence, the breakup type is vibrational.[36,40] Even an increase in solid nanoparticle concentration inside the 50 μm droplets does not affect the disintegration process. Therefore, droplet vaporization is dominant and controls the process when solid nanoparticles suspended in the droplets are injected with a small constant diameter of 50 μm.

In case 2.2 as droplet diameter increases to 150 μm the droplet's disintegration is reflected by the reduction of droplet diameter from 150 to 35 μm and from 35 to 13 μm inside the CC of the spray gun (Figure 8a–d). The Weber number varies from 25 to 30 depending on the nanoparticle concentration in the droplets and leads to severe fragmentation in the middle of the CC (Figure 8e–h). For all concentrations, the droplets get evaporated in the middle of the barrel and release solid nanoparticles, except for the highest concentration of 25 wt %. These high concentration droplets faced a delay in their evaporation process and reached the exit of the barrel. Similar results are observed for larger droplet diameter reductions (300 μm) while the *We* increases from 50 to 70 for constant diameter case 2.3. The above analysis indicates that the fragmentation process is dominant for large droplets (150 and 300 μm) while the rate of evaporation is higher for small droplets (50 μm). For brevity, case 2.3 and corresponding

DOI: 10.1021/acs.iecr.5b03956
Ind. Eng. Chem. Res. 2016, 55, 2556–2573

figures of droplet diameter reduction and Weber number variation are not included.

Figure 9a–h compares droplet evaporation for ST injection of 50 and 150 μm droplets with 0, 5, 15, and 25 wt % nanoparticle concentrations. The significance of droplet evaporation in the CC of the HVSFS torch is evident. It can be seen in Figure 9 that the maximum rate of evaporation occurs inside the CC while the final location of droplet evaporation stretches to the gun exit for the droplets carrying higher concentrations. The possible reason for this is the increase in the heat capacity (high required heat of vaporization) of the higher concentration droplets. It takes longer to reach the boiling point that leads to a lower vaporization in the CC.

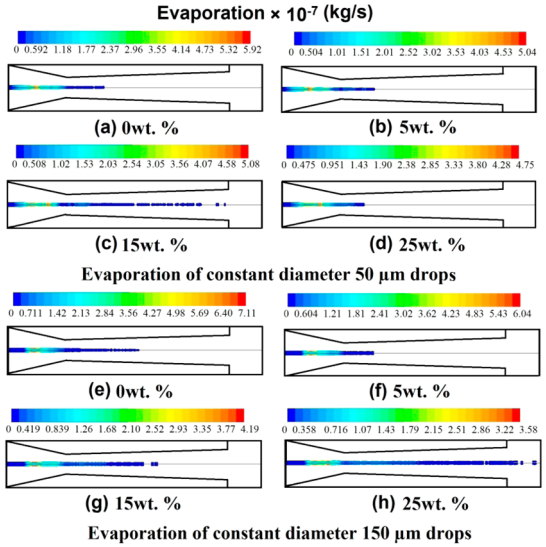

Figure 9. Evaporation rates of drops inside the domain for surface-type injection with constant diameters of (a–d) 50 and (e–h) 150 μm, having 0, 5, 15, and 25 wt % nanoparticle concentrations.

Moreover, larger droplets (150 μm) with a high concentration (25 wt %) leave the gun without complete vaporization (Figure 9e–h). It can lead to serious consequences in real applications and can create defects in the final coating. Delay in evaporation of the suspension droplets causes insufficient heating of suspended nanoparticles that may deposit without prior melting. It causes the inclusion of unmelted particles which leads to porosity.[19,32,60] It is inferred that, by increasing the percentage concentrations of nanoparticles in the base fluid, the rate of evaporation decreases, which causes a delay in the complete vaporization of droplets. However, small droplets get completely evaporated in the middle of the barrel. The implication is that small droplets can be effectively used in applications where the suspension contains nanoparticles with a high melting point, for example, coating applications with high melting point materials.

3.2.1.2. Varied Diameter Droplet Injection. Considerable reduction in diameter is observed for case 2.4, when drop streams with five different diameters (30, 40, 50, 60, and 70 μm) are injected into the gun (see Figure 10a–d). For these cases, the reduction is dependent on the injected size of droplets. For droplets with 30 μm diameters the reduction is from 20 to 14 μm and from 14 to 7 μm, and for 40 μm droplets, this reduction is from 30 to 20 μm and from 20 to 14 μm. Moreover, for larger drops of 60 μm diameter, a sharp decrease from 56 to 25 μm and from 25 to 18 μm is observed, and for 70 μm this reduction is even greater, from 66 to 30 μm and from 30 to 24 μm. This scenario of decreasing diameters for different initial drop sizes illustrates the higher fragmentation for drops larger than 50 μm and lower fragmentation for drops smaller than 50 μm.

The Weber number (We) for these different diameter droplets (30–70 μm) injection is presented in Figure 10e–h. Due to the presence of drops with varied sizes, droplet fragmentation is observed at varying positions along the axis. Varied diameter droplets carrying different nanoparticle concentrations have values of We < 14, and they have similar

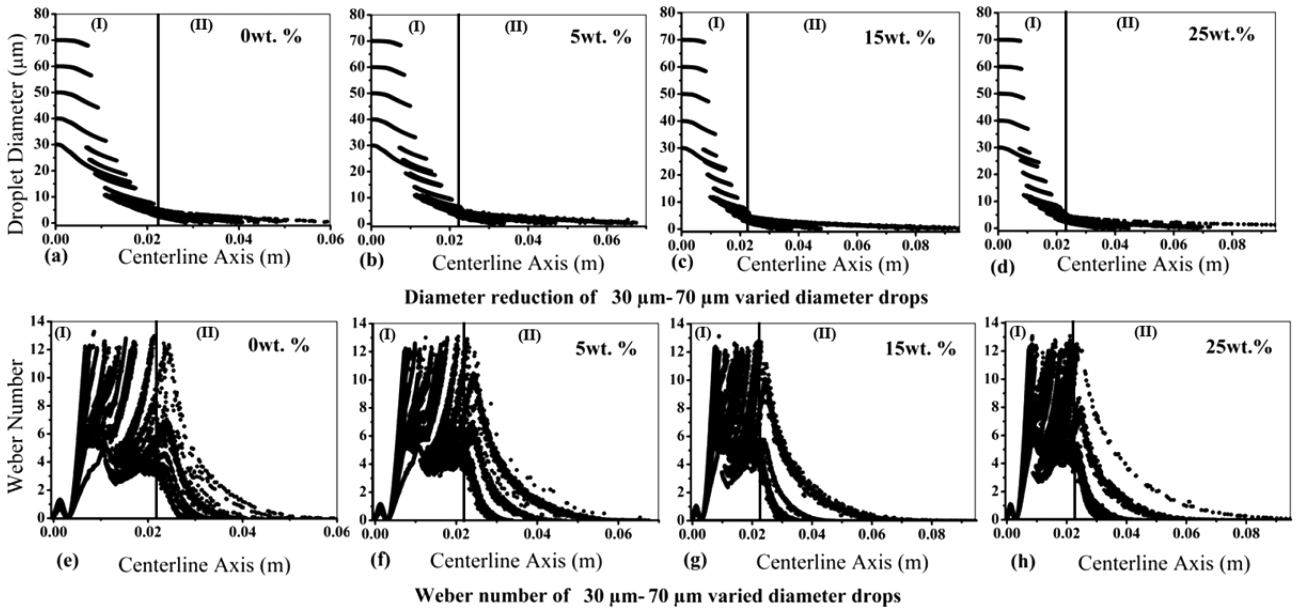

Figure 10. Comparison of (a–d) droplet diameter reduction and (e–h) Weber number for surface-type injection with varied diameters of 30, 40, 50, 60, and 70 μm, having 0, 5, 15, and 25 wt % nanoparticle concentrations.

DOI: 10.1021/acs.iecr.5b03956
Ind. Eng. Chem. Res. 2016, 55, 2556–2573

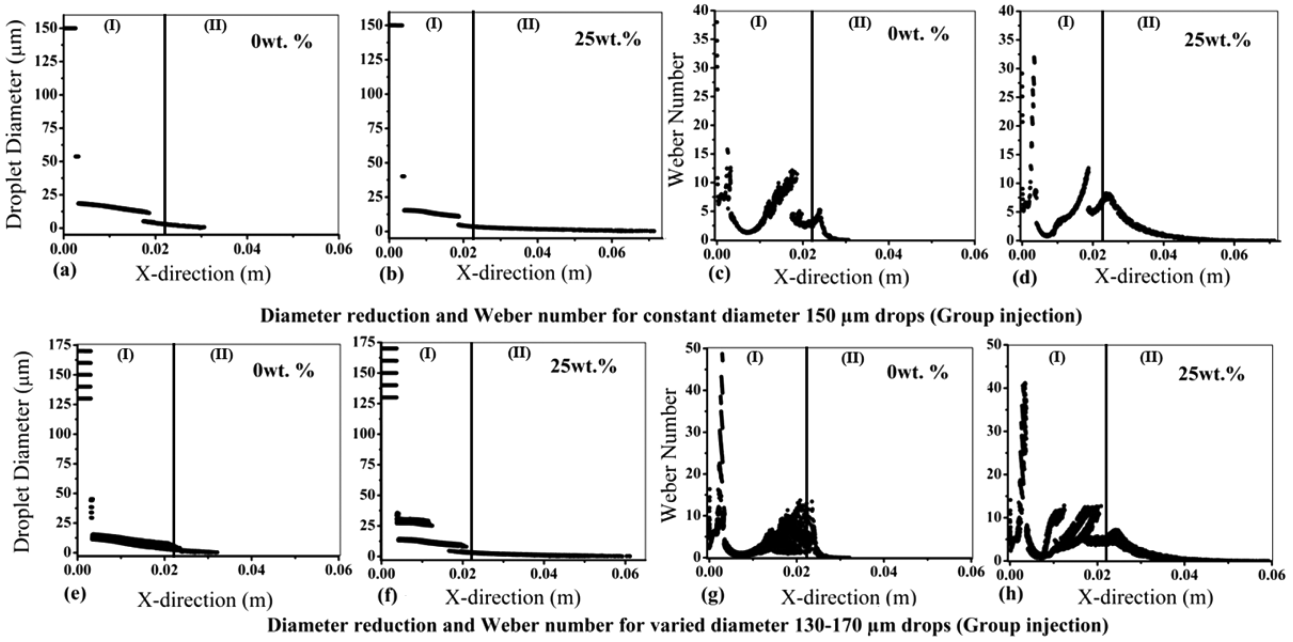

Figure 11. Comparison of droplet diameter reduction and droplet *We* number for group injection with a constant diameter of (a−d) 150 μm and with varied diameters of (e−h) 130, 140, 150, 160, and 170 μm, having 0 and 25 wt % nanoparticle concentrations.

vibrational type breakups[36,40] as observed for constant diameter drops of 50 μm (case 2.1).

When injected droplets have sizes varied from 130 to 170 μm (case 2.5) and from 280 to 320 μm (case 2.6), a similar trend in the results is noticed. It may be noted that the figures for these results are not included for brevity. In case 2.5, 71% reduction is noticed in the droplet size for all four different concentrations. In these cases, *We* fluctuates between 26 and 35 and severe fragmentation is observed inside the CC. Further, an increase in the nanoparticle concentration influences the disintegration and the evaporation process of drops; hence, droplets exit the gun without complete evaporation. The reduction in diameter for the larger droplets, with size varied from 280 to 320 μm (case 2.6), is 85%, and it is the highest in comparison to all other cases. Moreover, *We* increases from 55 to 80, proving that large droplets experience severe fragmentation inside the combustion chamber. Overall, it is noticed that when the Rosin−Rammler diameter distribution is applied to the ST injection, then more droplets discharge through the torch without prior evaporation. This complication intensifies with an increase in the nanoparticle concentration.

3.2.2. Group-Type Injection. 3.2.2.1. Constant Diameter Droplet Injection. The diameter reduction for GT injection is also significant, and an augmentation in the diameter reduction is detected with increasing injection diameter (case 3.2). It is further increased by increasing the nanoparticle concentration from 0 to 25 wt % as shown in Figure 11a,b. The reduction in diameters of constant size drops (150 μm) with 0 wt % nanoloading equals 65% (from 150 to 52 μm), and for 25 wt % nanoloading it is 74% (from 150 to 40 μm). The value of maximum *We* for case 3.2 is decreased from 38 to 32 for 0 and 25 wt % concentrations of nanoparticles, respectively (see Figure 11c,d). When compared with the ST injection (case 2.2) the higher values of *We* are observed for GT injection (case 3.2), and it proves that droplet disintegration is increased up to 34%.

3.2.2.2. Varied Diameter Droplet Injection. The reduction in diameter and the values of *We* are changed when GT injection of varied size drops is examined in case 3.5. As shown in Figure 11e,f, the reduction in diameter for the 0 wt % nanoparticle concentration is 70% (170−47 μm). However, diameter reduction of the 25 wt % concentration droplets is 79%. The maximum reduction is witnessed inside the CC, and droplets completely evaporate before escaping the gun. The maximum *We* for these extreme cases, having 0 and 25 wt % concentrations, changes from 50 to 42 (Figure 11g−h. The droplet deformations detected for the GT injection with the varied droplet diameter are significantly higher than for the case 2.5 with ST injection (carrying various diameter droplets).

Evaporation rates for group injection are shown in Figure 12. It is perceived by these trends that nanoparticle concentration has to be controlled to increase the efficiency of the evaporation process. The drops with constant diameters and having a lower nanoparticle concentration are evaporated in the barrel section (Figure 12a−c). When droplets are loaded with 25 wt % nanoparticles, they reach the end of the barrel before prior evaporation (Figure 12d). The highest evaporation rates are observed in all cases with constant diameter droplets delivered through the GT injection. It can be detected that varied size droplets also leave the nanoparticles in the middle of the barrel while the rate of evaporation is reduced (Figure 12e,f; 78% reduction for 25 wt %). Moreover, the group injection of constant diameter droplets and varied size drops with an injection angle of 45° work efficiently for smaller droplets (diameter $\leq$ 50 μm) having a small nanoparticle concentration (0−5 wt %). On the contrary, droplets with a diameter greater than 50 μm and having a high nanoparticle concentration of 15−25 wt % strike the walls of the CC and move forward along the walls of the torch. It must be avoided by using the proper angle of injection and injection velocities.

In summary, if the small size droplet (diameter $\leq$ 50 μm) injection is favored in an application, the extra liquid surfactant should be added to the suspension for reducing the drops'

DOI: 10.1021/acs.iecr.5b03956
Ind. Eng. Chem. Res. 2016, 55, 2556−2573

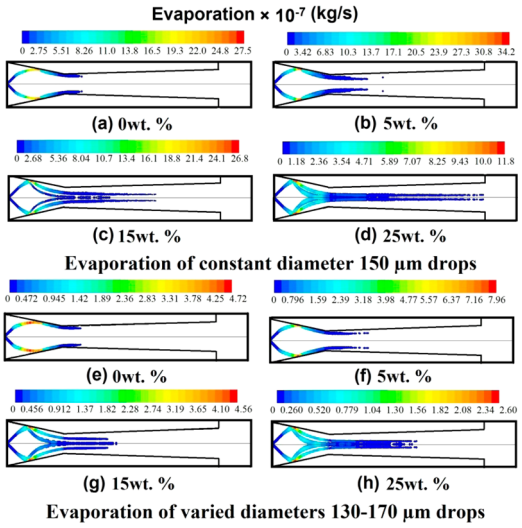

Figure 12. Evaporation rates of drops inside the domain for group injection with a constant diameter of (a–d) 150 μm and with varied diameters of (e–h) 130–170 μm, having 0, 5, 15, and 25 wt % nanoparticle concentrations.

surface tension and intensifying the fragmentation process. However, regarding droplet atomization in the HVSFS process, larger droplets lead to severe breakup with less evaporation when carrying higher nanoparticle concentrations. To increase the effectiveness of the HVSFS process, injection with smaller droplets is required with an optimized range of nanoparticle concentration. It is clear that the large size suspension droplets delay the droplet evaporation rate. This delay in the suspension evaporation would decrease the residence time of the solid particles inside the flame that increases the number of unmelted particles over the substrate. The increase in the unmelted nanoparticles can cause augmentation in the coating porosity. Hence, to form a defect-free coating, the smaller size suspension droplets would be used for completing the evaporation process of the suspension and better melting of solid nanoparticles before the deposition. For group-type injection, optimization is required for selecting the injection angle and the injection velocity with varying sizes of droplets to obtain the best results for the thermal spraying process.

It should be noted that, in the original design of the DJ2700 gun, the gas carrier tube is located at the center of the back wall, and it is surrounded by annular oxygen/fuel (O/F) inlets. It creates a recirculation zone close to the back wall at the injection area, and the particles start to spread out near the nozzle throat where the flame reaches the axis of the torch and interacts with the droplets. Likewise, when droplets injected at an angle of 45° are directed toward the combustion core, they have direct interaction with the flame which makes the evaporation process more effective in comparison to the axial injection. For this procedure, one has to control the injection parameters and fix them to avoid droplet collision with the combustion chamber walls.

Practically, a spray cone with a variety of droplet diameters is injected into a thermal spray gun. It causes velocity oscillations due to the unsteady nature of the HVSFS jet. These oscillations create droplets in any part of the domain from submicrometers to tens of micrometers in diameter. Due to fluctuations of the velocity field, droplets with a larger diameter can move toward the low-velocity jet area and may not experience aerodynamic fragmentation. Moreover, the amount of large droplets may not be fragmented as efficiently as others, resulting in the existence of bigger droplets tens of micrometers in size. Special care must be taken when injecting large droplets in the HVSFS process.

In the HVSFS process, the coating efficiency is dependent on the torch operating parameters as well as on the suspension's injection parameters. The in-flight behavior of suspension droplets, including the breakup and evaporation, has a strong link with the deposition efficiency. Hence, the complete evaporation of droplets inside the CC leads to sufficient heating and melting of suspended nanoparticles, and a fine coating can be achieved. More work is required to understand the effects of liquid feedstock atomization and vaporization on the coating structures.

4. CONCLUSION

Thermophysical properties of liquid fuel droplets with various solid nanoparticle concentrations (0, 5, 15, and 25 wt %) are calculated and modified based on the proposed models in the literature and then inserted into the models employed in this study. Subsequently, the effects of nanoparticle suspension on the gas dynamics and droplet dynamics (secondary breakup and vaporization rate) inside the HVSFS process are investigated. The main conclusions are as follows:

- The final location of evaporation is significantly changed for pure ethanol and suspension droplets (homogeneous and nonhomogeneous droplets). During the simulations, the nanoparticles are created in the computational domain as new entities; hence, the final location of evaporation is an important aspect of the numerical analysis of suspension droplets in the HVOF torch.
- Droplets with higher concentration have greater surface tension and require higher heat of vaporization; thus, an increase in the nanoparticle concentration delays the evaporation process of the droplets and adversely affects their disintegration.
- For surface-type and group-type injections, the effect on droplet breakup and evaporation is dependent on two parameters, namely (1) increasing the nanoparticle concentration and (2) increasing the droplet diameter. The rate of evaporation and the reduction in diameter are reduced with the increase in droplet size and nanoparticle concentrations.
- Smaller droplets ($d \leq 50$ μm) show a better trend for high concentration loading, as they experience high evaporation in the midsection of the nozzle and can be effectively used in applications where the suspension contains nanoparticles having a high melting point. The injection of smaller diameter droplets would improve the evaporation of suspension droplets and heating/melting of the solid content.
- For larger droplets (150 and 300 μm), fragmentation is the dominant factor that controls the process. Moreover, the larger droplets with high concentration leave the gun without complete vaporization. This can lead to serious consequences in real applications and can create defects in the final coating.
- The delay in the evaporation of larger droplets carrying higher nanoparticle concentration causes insufficient heating of the suspended nanoparticles, and they may be deposited without prior melting. These unmelted particles can create defects and result in augmentation in the coating porosity.
- The droplets added using group-type injections (at an angle of 45°) are inserted into the core of the combustion zone and reach the evaporation point rapidly in comparison to the surface-type injection (at an angle of 0°), and they evaporate completely inside the torch.

DOI: 10.1021/acs.iecr.5b03956
Ind. Eng. Chem. Res. 2016, 55, 2556–2573

- The group-type injection increases the efficiency of droplet disintegration and evaporation, and the effects of gas cooling are reduced.
- For increasing the effectiveness of group-type injection, optimized values of angles of injection, injection diameter, and injection velocity are required to avoid droplet collision with the torch combustion chamber walls.

AUTHOR INFORMATION

Corresponding Author

*E-mail: sai.gu@surrey.ac.uk. Tel.: +44 01483 682676.

Notes

The authors declare no competing financial interest.

ACKNOWLEDGMENTS

The authors would like to acknowledge the financial support by the U.K. Engineering and Physical Sciences Research Council (EPSRC) project grant EP/K027530/1, FP7 IPACTS Grant (268696), and the research studentship from the NED University of Engineering and Technology, Pakistan.

ABBREVIATIONS

CC	combustion chamber
C−D	convergent−divergent
CFD	computational fluid dynamics
DJ	diamond jet
GT	group type
HVSFS	high-velocity suspension flame spray
HVOF	high-velocity oxygen fuel
TAB	Taylor analogy breakup
ST	surface type

NOMENCLATURE

Symbols

A_d = area of droplet (m^2)
c_d = heat capacity of droplet ($J \cdot kg^{-1} \cdot K^{-1}$)
c_∞ = heat capacity of gas ($J \cdot mol^{-1} \cdot K^{-1}$)
$C_{i,s}$ = vapor concentration at droplet surface ($kg \cdot mol^{-1} \cdot m^{-3}$)
$C_{i,\infty}$ = vapor concentration in bulk gas ($kg \cdot mol^{-1} \cdot m^{-3}$)
C = volume concentration of solid particles in suspension
$\overline{d}$ = mean diameter (μm)
dm_d/dt = rate of evaporation ($kg \cdot s^{-1}$)
d = droplet diameter (μm)
h = convective heat transfer coefficient ($W \cdot m^{-2} \cdot K^{-1}$)
k_∞ = thermal conductivity of the gas ($W \cdot m^{-1} \cdot K^{-1}$)
k_p = thermal conductivity of titania powder ($W \cdot m^{-1} \cdot K^{-1}$)
k_l = thermal conductivity of base fluid (ethanol) ($W \cdot m^{-1} \cdot K^{-1}$)
$Kn = \lambda/d_d$ = Knudsen number (Kn)
k_c = mass transfer coefficient
L = latent heat ($J \cdot kg^{-1}$)
m_d = mass of droplet (kg)
M_w = molecular weight of species
N_i = molar flux of vapor
n = spread parameter
$Oh = \frac{\mu}{\sqrt{\rho \sigma d}}$ = Ohnesorge number (Oh)
$Re = \frac{\rho_c v_{rel}^2 d}{\mu}$ = Reynolds number (Re)
t = time (s)
T_{vap} = solvent evaporation temperature (K)
T_d = droplet temperature (K)
T_{boil} = droplet boiling temperature (K)
T_∞ = combustion gas temperature (K)
v_{rel} = relative velocity of droplets ($m \cdot s^{-1}$)
$We = \frac{\rho_c v_{rel}^2 d}{\sigma}$ = Weber number (We)
$Y_d = e^{-(d/\overline{d})^n}$ = mass fraction of droplets

Greek Symbols

μ = droplet viscosity ($kg \cdot m^{-1} \cdot s^{-1}$)
ρ_d = droplet density ($kg \cdot m^{-3}$)
ρ_c = combustion gas density ($kg \cdot m^{-3}$)
ρ_l = density of liquid ethanol ($kg \cdot m^{-3}$)
ρ_p = density of solid titania particles ($kg \cdot m^{-3}$)
ρ_{susp} = suspension density ($kg \cdot m^{-3}$)
σ = droplet surface tension ($N \cdot m^{-1}$)
λ = gas mean free path (m)

Subscripts

boil = boiling
c = combustion gas
d = droplet
i = species
l = liquid
p = particle
rel = relative
susp = suspension
vap = vaporization
∞ = free stream condition

REFERENCES

(1) Killinger, A.; Kuhn, M.; Gadow, R. High-Velocity Suspension Flame Spraying (HVSFS), a New Approach for Spraying Nano-particles with Hypersonic Speed. *Surf. Coat. Technol.* **2006**, *201*, 1922.

(2) Dobbins, T. A.; Knight, R.; Mayo, M. J. HVOF Thermal Spray Deposited Y2O3 -Stabilized ZrO2 Coatings for Thermal Barrier Applications. *J. Therm. Spray Technol.* **2003**, *12*, 214.

(3) Gell, M.; Jordan, E. H.; Teicholz, M.; Cetegen, B. M.; Padture, N. P.; Xie, L.; Chen, D.; Ma, X.; Roth, J. Thermal Barrier Coatings Made by the Solution Precursor Plasma Spray Process. *J. Therm. Spray Technol.* **2008**, *17*, 124.

(4) Pawlowski, L. Suspension and Solution Thermal Spray Coatings. *Surf. Coat. Technol.* **2009**, *203*, 2807.

(5) Gozali, E.; Kamnis, S.; Gu, S. Analysis of Liquid Feedstock Behavior in High Velocity Suspension Flame Spraying for the Development of Nanostructured Coatings. In *Proceedings of the International Thermal Spray Conference*; ASM International: Materials Park, OH, USA, 2013; pp 418−423.

(6) Gozali, E.; Kamnis, S.; Gu, S. Numerical Investigation of Combustion and Liquid Feedstock in High Velocity Suspension Flame Spraying Process. *Surf. Coat. Technol.* **2013**, *228*, 176.

(7) Espallargas, N. *Future Development of Thermal Spray Coatings: Types, Designs, Manufacture and Applications*, 1st ed.; Elsevier: London, 2015.

(8) Oberste Berghaus, J.; Legoux, J. G.; Moreau, C.; Hui, R.; Decès-Petit, C.; Qu, W.; Yick, S.; Wang, Z.; Maric, R.; Ghosh, D. Suspension HVOF Spraying of Reduced Temperature Solid Oxide Fuel Cell Electrolytes. *J. Therm. Spray Technol.* **2008**, *17*, 700.

(9) Oberste Berghaus, J.; Marple, B. R. High-Velocity Oxy-Fuel (HVOF) Suspension Spraying of Mullite Coatings. *J. Therm. Spray Technol.* **2008**, *17*, 671.

(10) Stiegler, N.; Bellucci, D.; Bolelli, G.; Cannillo, V.; Gadow, R.; Killinger, A.; Lusvarghi, L.; Sola, A. High-Velocity Suspension Flame Sprayed (HVSFS) Hydroxyapatite Coatings for Biomedical Applications. *J. Therm. Spray Technol.* **2012**, *21*, 275.

(11) Sampath, S. Thermal Spray Applications in Electronics and Sensors: Past, Present, and Future. *J. Therm. Spray Technol.* **2010**, *19*, 921.

DOI: 10.1021/acs.iecr.5b03956
Ind. Eng. Chem. Res. 2016, 55, 2556−2573

(12) Bolelli, G.; Cannillo, V.; Gadow, R.; Killinger, A.; Lusvarghi, L.; Rauch, J.; Romagnoli, M. Effect of the Suspension Composition on the Microstructural Properties of High Velocity Suspension Flame Sprayed (HVSFS) Al2O3 Coatings. *Surf. Coat. Technol.* **2010**, *204*, 1163.
(13) Fauchais, P.; Joulia, A.; Goutier, S.; Chazelas, C.; Vardelle, M.; Vardelle, A.; Rossignol, S. Suspension and Solution Plasma Spraying. *J. Phys. D: Appl. Phys.* **2013**, *46*, 224015.
(14) Fauchais, P.; Montavon, G. Latest Developments in Suspension and Liquid Precursor Thermal Spraying. *J. Therm. Spray Technol.* **2010**, *19*, 226.
(15) Dongmo, E.; Gadow, R.; Killinger, A.; Wenzelburger, M. Modeling of Combustion as Well as Heat, Mass, and Momentum Transfer during Thermal Spraying by HVOF and HVSFS. *J. Therm. Spray Technol.* **2009**, *18*, 896.
(16) Dongmo, E.; Killinger, A.; Wenzelburger, M.; Gadow, R. Numerical Approach and Optimization of the Combustion and Gas Dynamics in High Velocity Suspension Flame Spraying (HVSFS). *Surf. Coat. Technol.* **2009**, *203*, 2139.
(17) Dongmo, E.; Wenzelburger, M.; Gadow, R. Analysis and Optimization of the HVOF Process by Combined Experimental and Numerical Approaches. *Surf. Coat. Technol.* **2008**, *202*, 4470.
(18) Basu, S.; Cetegen, B. M. Modeling of Liquid Ceramic Precursor Droplets in a High Velocity Oxy-Fuel Flame Jet. *Acta Mater.* **2008**, *56*, 2750.
(19) Bolelli, G.; Rauch, J.; Cannillo, V.; Killinger, A.; Lusvarghi, L.; Gadow, R. Microstructural and Tribological Investigation of High-Velocity Suspension Flame Sprayed (HVSFS) Al2O3 Coatings. *J. Therm. Spray Technol.* **2009**, *18*, 35.
(20) Gell, M.; Jordan, E. H.; Teicholz, M.; Cetegen, B. M.; Padture, N. P.; Xie, L.; Chen, D.; Ma, X.; Roth, J. Thermal Barrier Coatings Made by the Solution Precursor Plasma Spray Process. *J. Therm. Spray Technol.* **2008**, *17*, 124.
(21) Bemporad, E.; Bolelli, G.; Cannillo, V.; De Felicis, D.; Gadow, R.; Killinger, A.; Lusvarghi, L.; Rauch, J.; Sebastiani, M. Structural Characterisation of High Velocity Suspension Flame Sprayed (HVSFS) TiO2 Coatings. *Surf. Coat. Technol.* **2010**, *204*, 3902.
(22) Rauch, J.; Bolelli, G.; Killinger, A.; Gadow, R.; Cannillo, V.; Lusvarghi, L. Advances in High Velocity Suspension Flame Spraying (HVSFS). *Surf. Coat. Technol.* **2009**, *203*, 2131.
(23) Gozali, E.; Mahrukh, M.; Gu, S.; Kamnis, S. Numerical Analysis of Multicomponent Suspension Droplets in High-Velocity Flame Spray Process. *J. Therm. Spray Technol.* **2014**, *23*, 940.
(24) Gozali, E.; Mahrukh, M.; Gu, S.; Kamnis, S. Numerical Investigation on Effects of Nanoparticles on Liquid Feedstock Behavior in High Velocity Oxygen Fuel (HVOF) Suspension Spraying. *Surf. Coat. Technol.* **2015**, *280*, 370.
(25) Xuan, Y.; Roetzel, W. Conceptions for Heat Transfer Correlation of Nanofluids. *Int. J. Heat Mass Transfer* **2000**, *43*, 3701.
(26) Gao, J. W.; Zheng, R. T.; Ohtani, H.; Zhu, D. S.; Chen, G. Experimental Investigation of Heat Conduction Mechanisms in Nanofluids. Clue on Clustering. *Nano Lett.* **2009**, *9*, 4128.
(27) Tanvir, S.; Qiao, L. Surface Tension of Nanofluid-Type Fuels Containing Suspended Nanomaterials. *Nanoscale Res. Lett.* **2012**, *7*, 226.
(28) Moosavi, M.; Goharshadi, E. K.; Youssefi, A. Fabrication, Characterization, and Measurement of Some Physicochemical Properties of ZnO Nanofluids. *Int. J. Heat Fluid Flow* **2010**, *31*, 599.
(29) Chen, R. H.; Phuoc, T. X.; Martello, D. Effects of Nanoparticles on Nanofluid Droplet Evaporation. *Int. J. Heat Mass Transfer* **2010**, *53*, 3677.
(30) Xiong, H. B.; Qian, L. J.; Lin, J. Z. Simulation of Effervescent Atomization and Nanoparticle Characteristics in Radio Frequency Suspension Plasma Spray. *J. Therm. Spray Technol.* **2012**, *21*, 226.
(31) Li, M.; Shi, D.; Christofides, P. D. Diamond Jet Hybrid HVOF Thermal Spray: Gas-Phase and Particle Behavior Modeling and Feedback Control Design. *Ind. Eng. Chem. Res.* **2004**, *43*, 3632.
(32) Bolelli, G.; Cannillo, V.; Gadow, R.; Killinger, A.; Lusvarghi, L.; Rauch, J. Properties of High Velocity Suspension Flame Sprayed (HVSFS) TiO2 Coatings. *Surf. Coat. Technol.* **2009**, *203*, 1722.
(33) Kamnis, S.; Gu, S. 3-D Modelling of Kerosene-Fuelled HVOF Thermal Spray Gun. *Chem. Eng. Sci.* **2006**, *61*, 5427.
(34) Kamnis, S.; Gu, S. Numerical Modelling of Propane Combustion in a High Velocity Oxygen−fuel Thermal Spray Gun. *Chem. Eng. Process.* **2006**, *45*, 246.
(35) Zeoli, N.; Gu, S.; Kamnis, S. Numerical Simulation of in-Flight Particle Oxidation during Thermal Spraying. *Comput. Chem. Eng.* **2008**, *32*, 1661.
(36) Zeoli, N.; Gu, S.; Kamnis, S. Numerical Modelling of Metal Droplet Cooling and Solidification. *Int. J. Heat Mass Transfer* **2008**, *51*, 4121.
(37) Kuo, K. *Principles of Combustion*, 2nd ed.; John Wiley & Sons, Inc.: 1986.
(38) Fukumoto, K.; Ogami, Y. Simulation of CO-H2-Air Turbulent Nonpremixed Flame Using the Eddy Dissipation Concept Model with Lookup Table Approach. *J. Combust.* **2012**, *2012*, 1.
(39) Magnussen, B. F.; Hjertager, B. H. On Mathematical Models of Turbulent Combustion with Special Emphasis on Soot Formation and Combustion. In *16th Symposium on Combustion*; The Combustion Institute: 1976; Vol. *16*, pp 719−729.
(40) Tabbara, H.; Gu, S. A Study of Liquid Droplet Disintegration for the Development of Nanostructured Coatings. *AIChE J.* **2012**, *58*, 3533.
(41) Hu, D. *Comparison of Numerical and Experimental Results of Four Liquid Spray Combustors*. M.Sc. Thesis, Louisiana State University and Agriculture and Mechanical College, 2002.
(42) Bovat, P. M. *Computational Analysis of Water Atomization in Spray Desuperheaters of Steam Boilers*. M.Sc. Thesis, Rensselaer Polytechnic Institute, 2013.
(43) Kamnis, S.; Gu, S.; Lu, T. J.; Chen, C. Computational Simulation of Thermally Sprayed WC-Co Powder. *Comput. Mater. Sci.* **2008**, *43*, 1172.
(44) Ranz, W. E.; Marshall, W. R. Evaporation from Drops. Part I. *Chem. Eng. Prog.* **1952**, *48*, 141.
(45) Ranz, W. E.; Marshall, W. R. Evaporation from Drops. Part II. *Chem. Eng. Prog.* **1952**, *48*, 173.
(46) Fauchais, P. L.; Heberlein, J. V. R.; Boulos, M. I. *Thermal Spray Fundamentals*; Springer Science+Business: New York, 2014.
(47) Sobolev, V. V.; Guilemany, J. M.; Nutting, J. Gas-Particle Interactions during Spraying. In *High Velocity Oxy-Fuel Spraying Theory, Structure-Property Relationships and Applications*; Shrikant, J., Ed.; W. S. Maney and Son Ltd.: 2004; pp 29−61.
(48) Sobolev, V. V.; Guilemany, J. M.; Garmier, J. C.; Calero, J. A. Modelling of Particle Movement and Thermal Behaviour during High Velocity Oxy-Fuel Spraying. *Surf. Coat. Technol.* **1994**, *63*, 181.
(49) Drew, D. A.; Passman, S. L. In *Theory of Multicomponent Fluids*; Applied Mathematical Sciences 135; Marsden, J. E., Sirovich, L., Eds.; Springer: New York, 2000; pp 11−293.
(50) Einstein, A. Investigations on the Theory of the Brownian Movement. *Ann. Phys.* **1905**, *17*, 549.
(51) Hosseini, S. S.; Shahrjerdi, A.; Vazifeshenas, Y. A Review of Relations for Physical Properties of Nanofluids. *Aust. J. Basic Appl. Sci.* **2011**, *5* (10), 417.
(52) Murshed, S. M. S.; Leong, K. C.; Yang, C. Investigations of Thermal Conductivity and Viscosity of Nanofluids. *Int. J. Therm. Sci.* **2008**, *47*, 560.
(53) Kim, S. H.; Choi, S. R.; Kim, D. Thermal Conductivity of Metal-Oxide Nanofluids: Particle Size Dependence and Effect of Laser Irradiation. *J. Heat Transfer* **2007**, *129*, 298.
(54) Murshed, S. M. S.; Leong, K. C.; Yang, C. Enhanced Thermal Conductivity of TiO2—water Based Nanofluids. *Int. J. Therm. Sci.* **2005**, *44*, 367.
(55) Wang, B. X.; Zhou, L. P.; Peng, X. F. A Fractal Model for Predicting the Effective Thermal Conductivity of Liquid with Suspension of Nanoparticles. *Int. J. Heat Mass Transfer* **2003**, *46*, 2665.

DOI: 10.1021/acs.iecr.5b03956
Ind. Eng. Chem. Res. 2016, 55, 2556−2573

(56) Perry, R. H.; Green, D. W. *Perry's Chemical Engineers' Handbook*, 7th ed.; Maloney, J. O., Ed.; McGraw-Hill: 1997.
(57) González-Tello, P.; Camacho, F.; Vicaria, J. M.; González, P. A. A Modified Nukiyama-Tanasawa Distribution Function and a Rosin-Rammler Model for the Particle-Size-Distribution Analysis. *Powder Technol.* **2008**, *186*, 278.
(58) Bailey, A. G.; Balachandran, W.; Williams, T. J. The Rosin-Rammler Size Distribution for Liquid Droplet Ensembles. *J. Aerosol Sci.* **1983**, *14*, 39.
(59) Mugele, R. A.; Evans, H. D. Droplet Size Distribution in Sprays. *Ind. Eng. Chem.* **1951**, *43*, 1317.
(60) Shi, D.; Li, M.; Christofides, P. D. Diamond Jet Hybrid HVOF Thermal Spray: Rule-Based Modeling of Coating Microstructure. *Ind. Eng. Chem. Res.* **2004**, *43*, 3653.

DOI: 10.1021/acs.iecr.5b03956
Ind. Eng. Chem. Res. 2016, 55, 2556−2573